CrossMark

# SN 2018agk: A Prototypical Type Ia Supernova with a Smooth Power-law Rise in Kepler (K2)

Qinan Wang[1], Armin Rest[1,2], Yossef Zenati[1,54], Ryan Ridden-Harper[1,3], Georgios Dimitriadis[4,5], Gautham Narayan[6,7], V. Ashley Villar[8,9,10], Mark R. Magee[5], Ryan J. Foley[4], Edward J. Shaya[11], Peter Garnavich[12], Lifan Wang[13], Lei Hu[14], Attila Bódi[15,16], Patrick Armstrong[17], Katie Auchettl[4,18,19], Thomas Barclay[20], Geert Barentsen[21], Zsófia Bognár[15,16], Joseph Brimacombe[22], Joanna Bulger[23], Jamison Burke[24,25], Peter Challis[26], Kenneth Chambers[23], David A. Coulter[4], Géza Csörnyei[15], Borbála Cseh[15], Maxime Deckers[5], Jessie L. Dotson[27], Lluís Galbany[28], Santiago González-Gaitán[29], Mariusz Gromadzki[30], Michael Gully-Santiago[31], Ottó Hanyecz[15], Christina Hedges[21,27], Daichi Hiramatsu[24,25], Griffin Hosseinzadeh[26], D. Andrew Howell[24,25], Steve B. Howell[27], Mark E. Huber[23], Saurabh W. Jha[32], David O. Jones[4,55], Réka Könyves-Tóth[15], Csilla Kalup[15], Charles D. Kilpatrick[33], Levente Kriskovics[15], Wenxiong Li[34], Thomas B Lowe[23], Steven Margheim[35], Curtis McCully[24,25], Ayan Mitra[36,37], Jose A. Muñoz[38,39], Matt Nicholl[40], Jakob Nordin[41], András Pál[15,42,43], Yen-Chen Pan[44], Anthony L. Piro[45], Sofia Rest[1,46], João Rino-Silvestre[29], César Rojas-Bravo[4], Krisztián Sárneczky[15], Matthew R. Siebert[4], Stephen J. Smartt[47], Ken Smith[47], Ádám Sódor[15,16], Maximilian D. Stritzinger[48], Róbert Szabó[15,16,42], Róbert Szakáts[15], Brad E. Tucker[17,19,49], József Vinkó[15,31,42,50], Xiaofeng Wang[51,52], J. Craig Wheeler[31], David R. Young[47], Alfredo Zenteno[53], KaiCheng Zhang[51], and Gabriella Zsidi[15,42]

[1] Department of Physics and Astronomy, The Johns Hopkins University, Baltimore, MD 21218, USA; qwang75@jhu.edu
[2] Space Telescope Science Institute, Baltimore, MD 21218, USA
[3] School of Physical and Chemical Sciences Te Kura Matu, University of Canterbury, Private Bag 4800, Christchurch 8140, New Zealand
[4] Department of Astronomy and Astrophysics, University of California, Santa Cruz, CA 95064, USA
[5] School of Physics, Trinity College Dublin, The University of Dublin, Dublin 2, Ireland
[6] Department of Astronomy, University of Illinois at Urbana-Champaign, 1002 W. Green St., IL 61801, USA
[7] Center for Astrophysical Surveys, National Center for Supercomputing Applications, Urbana, IL 61801, USA
[8] Department of Astronomy & Astrophysics, The Pennsylvania State University, University Park, PA 16802, USA
[9] Institute for Computational & Data Sciences, The Pennsylvania State University, University Park, PA 16802, USA
[10] Institute for Gravitation and the Cosmos, The Pennsylvania State University, University Park, PA 16802, USA
[11] Astronomy Department, University of Maryland, College Park, MD 20742, USA
[12] University of Notre Dame, Notre Dame, IN 46556, USA
[13] Mitchell Institute for Fundamental Physics and Department of Physics and Astronomy, Texas A&M University, College Station, TX 77843, USA
[14] Purple Mountain Observatory, Chinese Academy of Sciences, 10 Yuanhua Road, Nanjing 210033, People's Republic of China
[15] Konkoly Observatory, CSFK, Konkoly-Thege M. ut 15-17, Budapest, 1121 Hungary
[16] MTA CSFK Lendület Near-Field Cosmology Research Group, 1121, Budapest, Konkoly Thege Miklós út 15-17, Hungary
[17] Mt Stromlo Observatory, The Research School of Astronomy and Astrophysics, Australian National University, ACT 2601, Australia
[18] School of Physics, The University of Melbourne, VIC 3010, Australia
[19] ARC Centre of Excellence for All Sky Astrophysics in 3 Dimensions (ASTRO 3D), Australia
[20] University of Maryland, Baltimore County, 1000 Hilltop Circle, Baltimore, MD 21250, USA
[21] Bay Area Environmental Research Institute, P.O. Box 25, Moffett Field, CA 94035, USA
[22] Coral Towers Observatory, Cairns, Australia
[23] Institute for Astronomy, University of Hawai'i, 2680 Woodlawn Drive, Honolulu, HI 96822, USA
[24] Department of Physics, University of California, Santa Barbara, CA 93106-9530, USA
[25] Las Cumbres Observatory, 6740 Cortona Drive, Suite 102, Goleta, CA 93117-5575, USA
[26] Center for Astrophysics | Harvard & Smithsonian, 60 Garden Street, Cambridge, MA 02138-1516, USA
[27] NASA Ames Research Center, Moffett Field, CA 94035, USA
[28] Institute of Space Sciences (ICE, CSIC), Campus UAB, Carrer de Can Magrans, s/n, E-08193 Barcelona, Spain
[29] CENTRA, Instituto Superior Técnico, Universidade de Lisboa, Av. Rovisco Pais 1, 1049-001 Lisboa, Portugal
[30] Astronomical Observatory, University of Warsaw, Al. Ujazdowskie 4, 00-478 Warszawa, Poland
[31] Department of Astronomy, University of Texas at Austin, 2515 Speedway, Stop C1400, Austin, TX 78712-1205, USA
[32] Department of Physics and Astronomy, Rutgers the State University of New Jersey, 136 Frelinghuysen Road, Piscataway, NJ 08854, USA
[33] Center for Interdisciplinary Exploration and Research in Astrophysics (CIERA), Northwestern University, Evanston, IL 60208, USA
[34] The School of Physics and Astronomy, Tel Aviv University, Tel Aviv 69978, Israel
[35] Gemini Observatory, NSF's NOIRLab, Casilla 603, La Serena, Chile
[36] School of Engineering and Digital Sciences, Nazarbayev University, Nur-Sultan, Kazakhstan
[37] Kazakh-British Technical University, Almaty, Kazakhstan
[38] Departamento de Astronomía y Astrofísica, Universidad de Valencia, E-46100 Burjassot, Valencia, Spain
[39] Observatorio Astronómico, Universidad de Valencia, E-46980 Paterna, Valencia, Spain
[40] Birmingham Institute for Gravitational Wave Astronomy and School of Physics and Astronomy, University of Birmingham, Birmingham B15 2TT, UK
[41] Institute of Physics, Humboldt-Universität zu Berlin, Newtonstr. 15, D-12489 Berlin, Germany
[42] ELTE Eötvös Loránd University, Institute of Physics, Pázmany Péter sétány 1/A 1117, Budapest, Hungary
[43] ELTE Eötvös Loránd University, Department of Astronomy, Pázmany Péter sétány 1/A 1117, Budapest, Hungary
[44] Graduate Institute of Astronomy, National Central University, 300 Jhongda Road, 32001 Jhongli, Taiwan
[45] The Observatories of the Carnegie Institution for Science, 813 Santa Barbara St., Pasadena, CA 91101, USA
[46] Department of Computer Science, Johns Hopkins University, Baltimore, MD 21218, USA
[47] Astrophysics Research Centre, School of Mathematics and Physics, Queen's University Belfast, Belfast BT7 1NN, UK
[48] Department of Physics and Astronomy, Aarhus University, Ny Munkegade 120, DK-8000 Aarhus C, Denmark
[49] National Centre for the Public Awareness of Science, Australian National University, Canberra, ACT 2611, Australia
[50] Department of Optics & Quantum Electronics, University of Szeged, Dóm tér 9, Szeged, 6720 Hungary
[51] Physics Department and Tsinghua Center for Astrophysics (THCA), Tsinghua University, Beijing 100084, People's Republic of China

[52] Beijing Planetarium, Beijing Academy of Science and Technology, Beijing 100044, People's Republic of China
[53] Cerro Tololo Inter-American Observatory, NSF's National Optical-Infrared Astronomy Research Laboratory, Casilla 603, La Serena, Chile

## Abstract

We present the 30 minutes cadence Kepler/K2 light curve of the Type Ia supernova (SN Ia) SN 2018agk, covering approximately one week before explosion, the full rise phase, and the decline until 40 days after peak. We additionally present ground-based observations in multiple bands within the same time range, including the 1 day cadence DECam observations within the first $\sim$5 days after the first light. The Kepler early light curve is fully consistent with a single power-law rise, without evidence of any bump feature. We compare SN 2018agk with a sample of other SNe Ia without early excess flux from the literature. We find that SNe Ia without excess flux have slowly evolving early colors in a narrow range ($g - i \approx -0.20 \pm 0.20$ mag) within the first $\sim$10 days. On the other hand, among SNe Ia detected with excess, SN 2017cbv and SN 2018oh tend to be bluer, while iPTF16abc's evolution is similar to normal SNe Ia without excess in $g - i$. We further compare the Kepler light curve of SN 2018agk with companion-interaction models, and rule out the existence of a typical nondegenerate companion undergoing Roche lobe overflow at viewing angles smaller than 45°.

*Supporting material:* data behind figures, machine-readable tables

## 1. Introduction

Type Ia supernovae (SNe Ia) serve as standardizable candles in modern cosmology, and their use as distance indicators led to the discovery of the accelerating expansion of the universe (e.g., Riess et al. 1998; Perlmutter et al. 1999), which can be explained by the widely accepted concept of dark energy, or some alternative theories such as modified gravity (e.g., see discussion in Joyce et al. 2015 and Nojiri et al. 2017).

It has been proposed that SNe Ia may come from multiple progenitor channels (e.g., Foley et al. 2010; Polin et al. 2019). Foley et al. (2010) further reveals that if the light curves of SNe Ia subtypes deviate slightly from Phillips' relation, there will be a non-negligible systematic bias. Another easy-to-imagine scenario is that, if the rate of different progenitor channels correlates with environmental parameters that are different in low- and high-$z$ galaxies, e.g., metallicity, galaxy age, and star formation history, then the fraction of these SNe Ia subtypes will vary with time. This evolution will introduce systematics into the luminosity–distance relation. In the next decade with the Roman Space Telescope and the Rubin Observatory coming online, the rapidly growing SNe Ia samples will largely reduce the statistical uncertainties in cosmological measurement as well as improve the photometric calibration, and therefore systematic biases such as evolution that are currently secondary will become an important source of uncertainty in cosmological analyses (Scolnic et al. 2014, 2018; Riess et al. 2019).

In general, SNe Ia are believed to come from thermonuclear explosions of CO white dwarfs (WDs) in binaries, although no "Branch-normal" SN Ia progenitor system has yet been detected in pre-explosion images (Maoz et al. 2014). The trigger for the thermonuclear runaway (TNR) process in SNe Ia is thought to occur when the WD reaches or approaches a critical mass limit, known as the Chandrasekhar limit, $M_{\rm ch} \sim 1.4\,M_\odot$ (in some models TNR could happen in a sub-Chandrasekhar scenario, see discussion below). Such a process can occur in either the single-degenerate (SD) model (Whelan & Iben 1973) or the double-degenerate (DD) model (Iben & Tutukov 1984) or other rare

channels (Kashi & Soker 2011; Kushnir et al. 2013; Pakmor et al. 2013, 2021; Ruiter 2020). In the common SD model, a central WD accretes matter from a companion star up to $M_{\rm ch}$, and once the carbon ignition occurs near the center, deflagration soon follows and transitions to a detonation. This process produces an SN Ia-like event (Nomoto 1982a; Livne & Arnett 1995; Li & Van den Heuvel 1997; Kromer et al. 2010; Moll & Woosley 2013; Maoz et al. 2014; Jha et al. 2019; Soker 2019). In the DD model, the TNR process occurs when two CO WDs or CO–HeCO merge via angular momentum loss by radiating gravitational waves (i.e., Dan et al. 2011; Perets et al. 2019).

The TNR process can occur at different stages depending on SN Ia progenitors: during mass transfer, during the merger, or in the remnant phase after the merger (Iben & Tutukov 1984; Livne & Glasner 1991; Fink et al. 2010; Guillochon et al. 2010; Pakmor et al. 2013; Dan et al. 2014; Kashyap et al. 2015; Perets et al. 2019; Polin et al. 2019). The ambiguity in the timing of the TNR process introduces more variation in modeling. For example, Nomoto (1982b) and Woosley et al. (1986) proposed the sub-Chandrasekhar double detonation (DDet) model, in which a detonation of the helium shell of the WD triggers a detonation of the carbon core. Other proposed models include the collision of double WDs (Kushnir et al. 2013), the explosion of a massive hybrid HeCO WD as a donor in the DD system (Zenati et al. 2019; Pakmor et al. 2021), and the core-degenerate model (merger of a WD and an asymptotic giant branch star, see Kashi & Soker 2011). All of these scenarios could give rise to the bulk of SNe Ia.

Clues to the progenitor systems of SNe Ia can be found through early observations of SN Ia light curves within days after explosion. The canonical "expanding fireball" model predicts that the early rise of the SNe Ia light curve follows $L \propto t^2$ under the assumption that the photospheric temperature remains roughly constant during this period (Arnett 1982; Riess et al. 1998). Previous observations have revealed that the rise of SNe Ia statistically follows a power law $L \propto t^\alpha$ with index $\alpha \sim 2$, though the index of some SNe Ia may deviate significantly from 2 (Riess et al. 1998; Hayden et al. 2010; Olling et al. 2015; Miller et al. 2020). Recently, some models further predict the existence of early excess on top of the power-law rise under some conditions. Kasen (2009) reveals that in the SD model the interaction between SN ejecta and a nondegenerate companion can produce a blue

---

excess in SN Ia light curves within days from explosion. In such SD models, H or He features are also expected to be found in late-phase spectra (Maeda et al. 2014; Botyánszki et al. 2018). Multiple mechanisms have also been proposed to be able to create a variety of flux excess in early SN Ia light curves in DD models afterwards. For example, Piro & Morozova (2016) shows that shock interaction with circumstellar medium can create similar excess to the SD model; in the sub-$M_{ch}$ DDet scenario, excess flux can be caused by an initial He detonation that ejects a non-negligible amount of radioactive isotopes on the surface and thus such events have a relatively red early excess (Kromer et al. 2010; Kushnir et al. 2013; Pakmor et al. 2013; Tanikawa et al. 2015; Noebauer et al. 2017; Perets et al. 2019; Ruiter 2020; Magee & Maguire 2020) due to Fe line blanketing (Maeda et al. 2018). For the DD scenario, Levanon et al. (2015) and Levanon & Soker (2017) show that if the merger process forms an accretion disk that blows a wind shortly before the explosion, then the collision of the ejecta with this disk-originated matter results in an early light excess. Overall, these various models give different predictions on the shape and color of the early flux excess. These early effects of different models highlight the importance of early observations, as has been proven through combinations of different pieces of observational evidence, including light curve shape, color evolution, and early spectra (Jha et al. 2019).

Continuous high-cadence surveys are a key window to precisely constrain explosion time and search for those potential photometric signatures of progenitors in the very early phase. With its wide field of view and 30 minutes cadence, the Kepler Space Telescope (Kepler; Haas et al. 2010) was a superb instrument for monitoring thousands of galaxies to observe SNe within hours of their explosion times. During the Kepler prime mission, Olling et al. (2015) discovered three photometrically classified SNe Ia with coverage from days before explosion to the post-peak phase, which do not have any signatures of early excess. The successor to the Kepler prime mission, K2 (Howell et al. 2014), had two campaigns (C16 and C17) dedicated to the K2 Supernova Cosmology Experiment (K2 SCE), during which the telescope monitored groups of low-redshift galaxies with concurrent ground-based observations. This program successfully monitored numerous SNe as well as other extragalactic transients (e.g., Rest et al. 2018).

K2 observed eight spectroscopically classified SNe Ia from pre-explosion to post-peak stage (A. Villar et al. 2021, in preparation). The most remarkable discovery was SN 2018oh, which featured a prominent early excess in the Kepler light curve for the first ~5 days after the explosion (Shappee et al. 2018; Li et al. 2019; Dimitriadis et al. 2019a). Both SD collision models and DD models with a shallow concentration of $^{56}$Ni can approximately reproduce the early Kepler light curve shape of SN 2018oh. Alongside early Kepler photometry, early measurements were also obtained with DECam in $i$. These data suggested an early blue excess, favoring the SD model. However, the color agreement is contradicted by late-time spectra that showed no evidence of hydrogen or narrow helium emission features that are predicted by the SD model (Tucker et al. 2019; Dimitriadis et al. 2019b). On the other hand, Magee & Maguire (2020) also reveals the inconsistency in late-time color and spectra between the observation and prediction of the shallow $^{56}$Ni model. Thus, no model can simultaneously match photometric and spectroscopic features of SN 2018oh at this stage.

Still, our ability to understand the excess flux in SNe Ia such as SN 2018oh is limited by not having a clear template and model to define "normal" flux and color evolution—i.e., an SN Ia without excess flux. A template SN Ia with early observations that contains no excess feature is crucial for understanding SNe Ia with excess flux and distinguishing between different progenitor models. Another problem in analysis is the existence of a "dark phase," referring to the time difference between the explosion and the occurrence of observable first light (Piro & Nakar 2013; Magee et al. 2020), and this still needs to be carefully evaluated in model simulations.

In this paper, we present observations of SN 2018agk, a "normal" SN Ia in both spectroscopic and photometric senses, whose host galaxy was monitored by the K2 SCE from pre-explosion to post-peak stage. We show that the Kepler light curve has no signature of early excess features. In addition, SN 2018agk was extensively observed by ground-based observatories in multiple bands, and in particular, DECam observed it at a ~1 day cadence from pre-explosion to ~4 days after the first light in $g$ and $i$ bands. In this paper, we focus on the Kepler and DECam light curve and color evolution within the first week after first light. With these unique multiband data, we are able to reveal the intrinsic color evolution of SNe Ia without excess. Furthermore, we use the Kepler light curve as a baseline to test previous model fitting methods.

Throughout this paper, observed times are reported in modified Julian days (MJDs), while phases, unless noted otherwise, are reported in the rest frame. We adopt the AB magnitude system, unless noted otherwise, and a flat $\Lambda$CDM cosmological model with $H_0 = 73$ km s$^{-1}$ Mpc$^{-1}$ (Riess et al. 2016, 2018).

## 2. Observations

SN 2018agk was discovered with the CTIO 4 m Blanco DECam camera (DePoy et al. 2008; Flaugher et al. 2015) on 2018 March 10 at 07:06:06 UTC (MJD 58,188.296) with apparent $g$-band magnitude of 20.235 mag (Rest et al. 2018). The images were taken by the Kepler ExtraGalactic Survey (KEGS) team as part of the ground-based monitoring of the K2 Campaigns 16 and 17 (Dotson et al. 2018). SN 2018agk occurred at coordinates $\alpha = 13^h10^m36^s.37$, $\delta = -04°29'08''.67$ (J2000.0) and was spectroscopically classified as an SN Ia by Bose et al. (2018). SN 2018agk is located at a distance of $8''.8$ from the center of its host galaxy, IC 0855, which is a spiral galaxy at a redshift of $z = 0.026128$ (see Figure 1). Throughout this paper, we use the Milky Way extinction of $E(B - V)_{MW} = 0.034$ from the extinction map as described in Schlafly & Finkbeiner (2011).

### 2.1. Ground-based Photometry

We obtained ground-based photometry with the CTIO 4 m Blanco telescope with DECam in $g$ and $i$ bands, the Swope 1.0 m telescope at Las Campanas Observatory in $uBVgri$ bands, the 60/90 cm Schmidt telescope on Piszkéstető Mountain Station of Konkoly Observatory in $BVRI$ bands, the 1.3 m telescope at the Cerro Tololo Inter-American Observatory (CTIO) in $RIJHK$ bands, and the PS1 1.8 m telescope at Haleakala on Maui, Hawai'i in $gri$ bands (Chambers et al. 2016). We also include photometric data from the Global Supernova Project taken with Las Cumbres Observatory previously published in Baltay et al. (2021). We downloaded the data products using the NSF NOIRLab DECam Community Pipeline (Valdes & Gruendl 2014). The standard
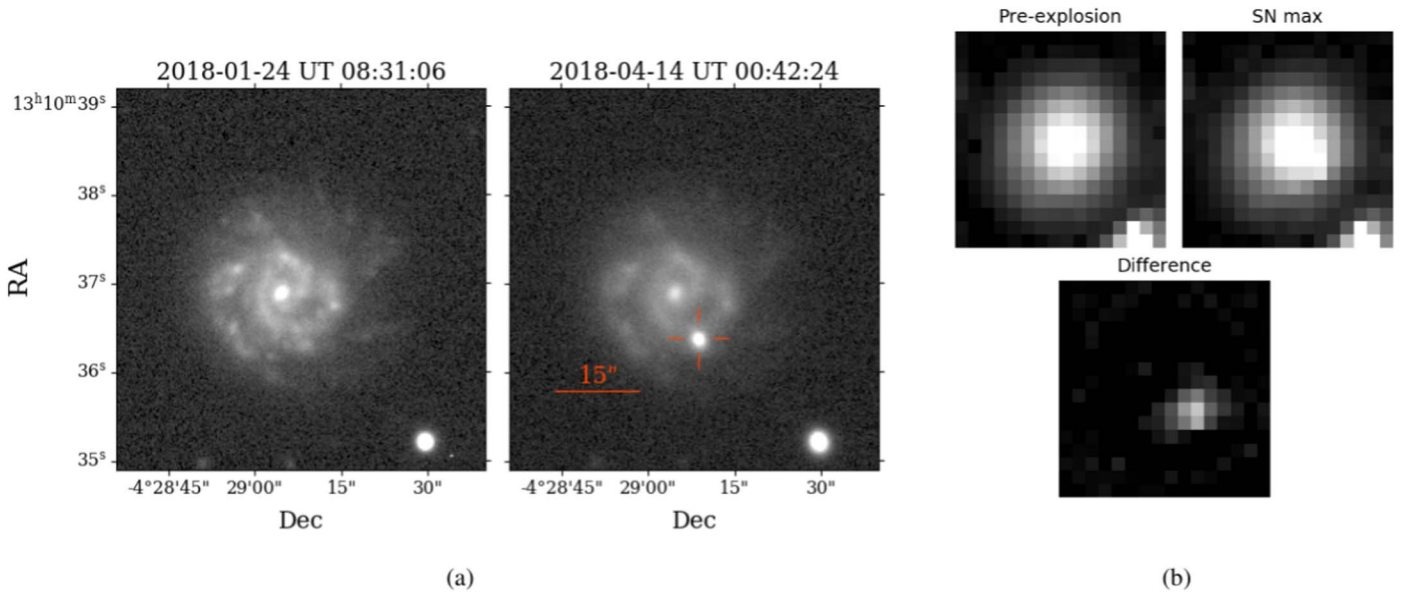
**Figure 1.** (a) The DECam $g$-band image of SN 2018agk and its host galaxy IC 0855 in the pre-explosion stage (left) and ~18 days after $B$-band maximum (right). The size of the two images is $64'' \times 64''$. (b) Kepler images of SN 2018agk and its host pre-explosion (top left), peak (top right), and the difference image (bottom). The size of the Kepler images is $16 \times 16$ pixels ($64'' \times 64''$).

reduction of the Swope images is described in Kilpatrick et al. (2018). We reduced the PS1 images using the standard PS1 Image Processing Pipeline (Magnier et al. 2020a, 2020b, 2020c; Waters et al. 2020), which includes standard reductions, astrometric solution, stacking of nightly images, source detection, and photometry. The photometry of all images was calibrated using standard sources from the Pan-STARRS DR1 catalog (Flewelling et al. 2020) in the same field as SN 2018agk and transformed following the Supercal method (Scolnic et al. 2015). After standard reductions, the `photpipe` pipeline (Rest et al. 2005, 2014) performs difference imaging and transient identification. DECam observed SN 2018agk during the crucial first five days after explosion, making it the first SN Ia that has both a high-cadence Kepler light curve and ground-based multiband observations in its earliest phase. DECam $g$-band images from well before explosion and ~20 days after peak are shown in Figure 1(a), and the full multiband light curves are plotted in Figure 8.

### 2.2. Kepler Observation

IC 0855 was included as a Campaign 17 target through "The K2 ExtraGalactic Survey (KEGS) for Transients" (PI Rest) and the "Multi-Observatory Monitoring of K2 Supernovae" (PI Foley) programs as part of the K2 SCE (internal Kepler EPIC ID 228682548). We retrieved the IC 0855 Kepler data through the Mikulski Archive for Space Telescopes (MAST) after the end of K2 Campaign 17.

The unstable pointing of Kepler throughout K2 required special treatment to reduce the data. The Kepler/K2 mission is characterized by a unique observing strategy that uses spacecraft geometry in conjunction with periodic thruster resets to maintain pointing. This strategy induced a short-scale periodic 6 hr "sawtooth pattern," alongside long-term sensitivity trends, due to differential heating on the spacecraft body and zodiacal background throughout a campaign.

To correct for short- and long-term trends, we first reduce the data using our K2 reduction pipeline, which is described in Shaya et al. (2015) in more detail. This method removes the sawtooth pattern by fitting a third-order polynomial in both spatial

dimensions of the centroid of the image to the pattern in the light curve of a fixed $5 \times 5$ pixel aperture. Long-term trends are removed making use of the vectors from our principal-component analysis (PCA) that characterize common simultaneous trends seen in the light curves of all the (assumed) non-varying galaxies observed on the same channel (chip). There were 293 galaxies on the same channel as SN2018agk. For supernovae, the applicable coefficients of the PCA vectors and the sawtooth function are estimated using only the times of no supernova flux at the beginning and/or end of the light curve. In this case, we do not have an end anchor point, so the reduced light curve may become unreliable for times significantly past the peak. This is not a significant hindrance to our analysis, as we only use the K2 light curve during the rise. After the long-term trends are divided out, we subtract the sawtooth pattern of the galaxy throughout the light curve. The remainder is the supernova light curve, which will generally have a sawtooth pattern of lower amplitude because it is a point source and thus has less of its light shifting in and out of the aperture than the galaxy. The sawtooth pattern can be scaled down to fit this and removed, but, for this supernova, this was not needed.

Finally, to remove the few outliers, we further model the smooth light curve with a Gaussian process regression (GPR) through the `celerite` package (Foreman-Mackey et al. 2017) and apply a $3\sigma$ cut, as shown in Figure 2. We used a Matérn 32 kernel with length scales of a few days, which will be insensitive to the short-timescale excursions caused by the K2 thruster resets. In the modeling we explored parameters of the GPR in a reasonable range to balance between rejecting obvious outliers and keeping reliable data in the rise phase for further analysis. From the smoothed light curve we find the peak in the K2 band occurs at $\mathrm{MJD}_{\mathrm{max}}^{\mathrm{K2}} = 58{,}203.78 \pm 0.02$. To estimate noise, we compute the rms variation of the background flux before the explosion and then scale it by the square root of the galaxy flux plus the SN flux in the aperture.

### 2.3. Ground-based Spectroscopy

We obtained a total of 17 spectra for SN 2018agk from ground-based observatories: one spectrum with the Gemini
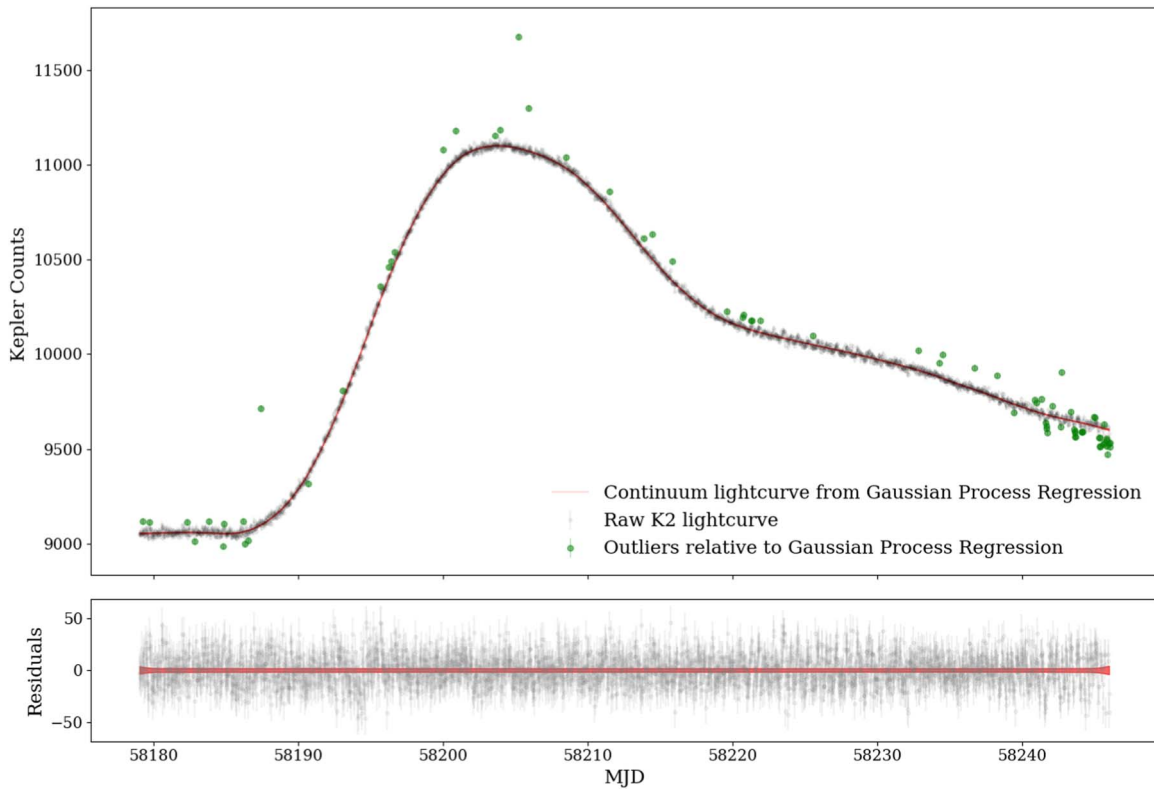
**Figure 2.** The processed Kepler light curve of SN 2018agk before and after a cut by Gaussian process regression (top panel) and residual differences (bottom panel). After pipeline reduction, instrumental systematics still have non-negligible influence on Kepler data, e.g., the discontinuities and outliers. We used GPR to remove the outliers and create a smoothed light curve to estimate the peak counts and time for later analysis. We tune the GPR parameter to balance between removing more outliers and keeping data in the fast-evolving early rise phase, and we find the optimal cutoff limit for residuals to be $3\sigma$.

(The data used to create this figure are available.)

Multi-Object Spectrograph (GMOS; Hook et al. 2004) on the Gemini-North telescope (GN-2018A-LP-13, PI: Garnavich); four spectra with ESO Faint Object Spectrograph and Camera (EFOSC2; Buzzoni et al. 1984) on the ESO New Technology Telescope (as part of the ePESSTO survey, Smartt et al. 2015); one spectrum with the Kast spectrograph (KAST; Miller & Stone 1993) on the Lick Shane telescope (2018A-S023, PI: Foley); two spectra with the Low-Resolution Imaging Spectrometer (LRIS; Oke et al. 1995) on the Keck I telescope (U240, PI: Foley); one spectrum with the Goodman High Throughput Spectrograph (Clemens et al. 2004) at the Southern Astrophysical Research (SOAR) Telescope (2018A-0277, PI: Foley); five optical spectra with the twin FLOYDS spectrographs mounted on Las Cumbres Observatory's 2 m Faulkes Telescopes North (FTN) at Haleakala Observatory in Hawai'i and Faulkes Telescopes South (FTS) at Siding Spring Observatory in Australia; and two spectra with the Low Resolution Spectrograph-2 (LRS2) (Chonis et al. 2016) on the 10 m Hobby–Eberly Telescope (HET) at McDonald Observatory, where the UV and Orange arms of the Blue Integral Field Unit were applied, resulting in a spectrum between 3640 and 6970 Å. We additionally use the publicly available classification spectrum, posted on the Transient Name Server (TNS), obtained with the Wide-Field CCD (WFCCD) of the 2.5 m du Pont Telescope at Las Campanas Observatory (Bose et al. 2018).

The spectra were reduced using standard IRAF/PYRAF and Python routines for bias/overscan subtractions and flat-fielding. The wavelength solution was derived using arc lamps while the

final flux calibration and removal of telluric lines were performed using spectrophotometric spectra of standard stars.

Spectra from Gemini-North, Shane KAST, Keck I LRIS, and SOAR were reduced using standard IRAF/PYRAF[56] and Python routines for bias/overscan subtractions and flat-fielding. The wavelength solution was derived using arc lamps while the final flux calibration and removal of telluric lines were performed using spectrophotometric spectra of standard stars. The EFOSC2 spectra were reduced in a similar manner, with the aid of the PESSTO pipeline.[57] The HET LRS2 spectra were reduced through custom-developed IRAF scripts (see Yang et al. (2020) for more details on the LRS2 IFU spectrograph and the reduction process). The FLOYDS spectra from Las Cumbres Observatory's FTS and FTN were reduced using standard IRAF tasks as described in Valenti et al. (2014). Table 3 in the Appendix summarizes our spectroscopic observations and Figure 3 shows the evolution of the spectra.

### 2.4. Hubble Space Telescope Observations

We triggered Hubble Space Telescope (HST) follow-up of SN2018agk on 2018 March 16 (GO-15274, PI Garnavich) and the first exposure began March 19 17:09 (UT). However, due to an HST gyro glitch, the visit failed after the first

---

[56] IRAF was distributed by the National Optical Astronomy Observatory, which was managed by the Association of Universities for Research in Astronomy (AURA) under a cooperative agreement with the National Science Foundation.
[57] https://github.com/svalenti/pessto
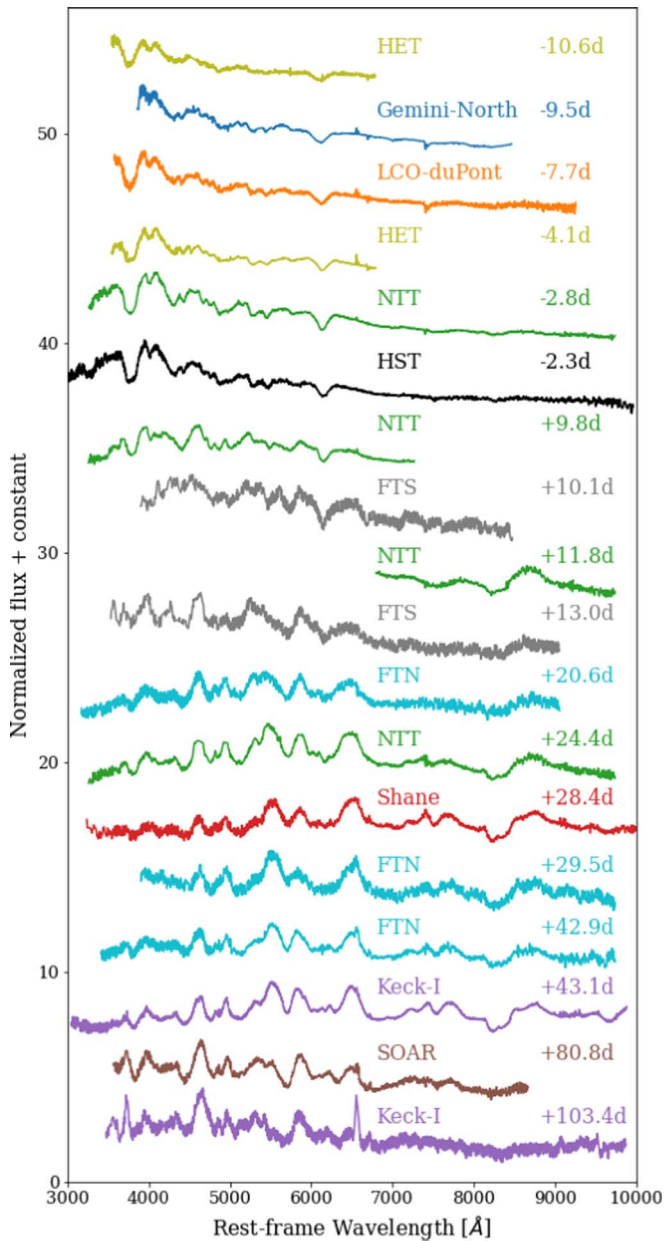
**Figure 3.** Spectral series of SN 2018agk. The phases are labeled above each spectrum, and spectra from different instruments are plotted with different colors. The HST spectra taken with three gratings on around MJD 58,201.8 (∼2.3 days before *B*-band maximum) have been combined into one. All the spectra have been shifted for better display.

(The data used to create this figure are available.)

exposure. A full complement of observations were obtained on the second visit five days later. During both visits, Space Telescope Imaging Spectrograph (STIS) spectra were obtained using the G230L grating and 0″2 wide slit using the NUV-MAMA detector. On the second visit, CCD spectra using the G430L and G750L gratings were obtained, providing wavelength coverage from 170 to 1010 nm. The spectra were extracted, wavelength-corrected, and flux-calibrated through the standard STIS pipeline, and are plotted in Figure 7 in contrast to the HST UV spectra of SN 2011fe taken around a similar phase.

## 3. Analysis

### 3.1. Spectroscopy

Branch et al. (2006) and Wang et al. (2009) showed that the pseudo-equivalent width (pEW) of the Si absorption lines (Si II $\lambda$6355 and Si II $\lambda$5972) and the velocity of the Si II $\lambda$6355 line around peak can be used to classify SNe Ia into different branches. Here we applied this classification scheme to SN 2018agk. To estimate pEW, we first define the pseudo-continuum $f_c(\lambda)$ by the linear curve connecting local maxima at the edge of the absorption features that does not intersect the spectral features. Then we integrate the flux normalized by the pseudo-continuum through the formula

$$\mathrm{pEW} = \int \frac{f_c(\lambda_i) - f(\lambda_i)}{f_c(\lambda_i)} dx \qquad (1)$$

where $f(\lambda_i)$ is the measured flux. We perform the integration using `scipy.integrate.quad`. We also measure the velocity of the Si II 6355 Å line by the blueshift of the absorption minimum in the spectrum normalized by the pseudo-continuum.

We do the calculation on the HST spectrum taken on MJD 58,201.90, ∼2.2 days prior to the *B*-band maximum, and measure the pEW of Si II $\lambda$6355 to be $92.621 \pm 0.009$ Å and that of Si II $\lambda$5972 to be $24.1 \pm 0.1$ Å. The velocity of Si II $\lambda$6355 is $-10,200 \pm 100$ km s$^{-1}$. The Branch diagram is plotted in Figure 4, in comparison to the sample from Blondin et al. (2012). It clearly shows that SN 2018agk matches the features of Branch-normal SNe Ia and does not have any peculiar features.

The spectroscopic evolution of SNe Ia forms a rather homogeneous family, which allows any individual SN Ia to be studied based on knowledge of the entire SN Ia sample. The data-driven model of the SNe Ia developed by Hu et al. (in 2021) is applied to the spectroscopic data of SN 2018agk. This model is based on the long short-term memory (LSTM) neural networks. The model can construct a complete spectral sequence of an SN Ia using spectroscopic data around optical maximum. For normal SNe Ia, the flux level of the entire spectral sequence can be reconstructed to a precision of better than 7%. The evolution of spectral features can also be predicted accurately. The left panel of Figure 5 shows the LSTM neural network projection of the spectral sequence of SN 2018agk. We picked two spectra with the highest signal-to-noise ratio (S/N) around peak, plotted in red, to build the projections, which are plotted as black lines. The remaining spectra with high S/N plotted in green are used to test the fidelity of the neural network projections. The bottom panel shows the ratios of the observations to the neural network projections. The predictions are good to a few percent in general. The phases of the spectra are shown in the color bars on the right. It can be seen that the spectral predictions match up to the earliest spectroscopic observations (day −9.5 from optical maximum) and down to around 1 month after the optical maximum can be very well reconstructed using only the spectra taken around and after optical maximum (days −2.8 and 9.8 from optical maximum). The success of this reconstruction again supports the notion that SN 2018agk is a member of well-observed SNe Ia that are used to build the LSTM neural network models. We further utilize the LSTM neural network projections to study the evolution of the blueshifts of the Si II $\lambda$6355 features, as shown in the right
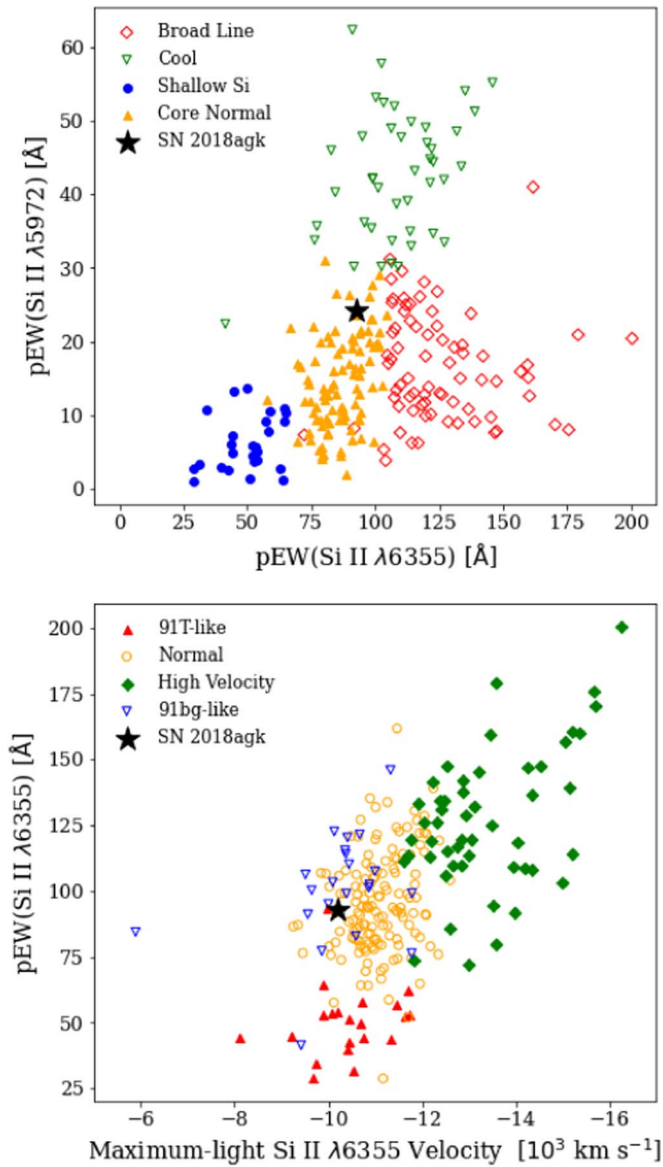
**Figure 4.** Classification diagram of the subtypes of SNe Ia as defined by Branch et al. (2006) and Wang et al. (2009). The pEW and velocity of Si lines in the HST spectra of SN 2018agk at 2.3 days before *B*-band maximum (black star) indicate that it is a normal SN Ia.

panel of Figure 5. The evolution trend of Si II λ6355 measured from the projected spectra of SN 2018agk has been plotted in Figure 6 against the projections of other SNe Ia from the same LSTM neural networks. The black line shows the velocity of SN 2018agk measured from the projected spectra and the black solid dots show the measured velocity from the observed spectra. In this figure we also plot normal SNe Ia (dotted lines) and the high-velocity group (dashed lines). SN 2018agk shows a strong similarity with the group of normal SNe Ia and validates our conclusion that it is a typical Branch-normal SN Ia.

We estimate the host extinction in the line of sight using the method from Poznanski et al. (2012). After correcting our highest resolution spectra for redshift, we fit the Na I D (λ5890) doublet and measure equivalent width EW = $0.75 \pm 0.15$ Å. Using Equation (9) from Poznanski et al. (2012), we estimate $E(B - V)_{\text{host}} = 0.11 \pm 0.05$.

Differences in SN Ia progenitor metallicity are theoretically expected to affect both the peak luminosity and UV spectral energy distribution (SED) of an SNe Ia while having minimal impact on the optical SED (e.g., Höflich et al. 1999; Lentz et al. 2000). The predicted trends have been observed in SNe Ia data (Foley & Kirshner 2013; Graham et al. 2015; Foley et al. 2016, 2020) and show a difference in UV continuum that correlates with shape-corrected luminosity (Foley et al. 2020) and host-galaxy metallicity (Pan et al. 2020). Since the exact model SED depends on the exact progenitor and explosion model, Foley & Kirshner (2013) used the flux ratio between Lentz et al. (2000) models with different metallicities compared to the flux ratio between different SNe to determine the relative metallicity of the SNe. We compare the reddening-corrected UV spectra of SN 2018agk at two epochs to phase-matched spectra of SN 2011fe, an SN Ia with a similar light-curve shape to SN 2018agk (Figure 7). In general, the UV spectra of two SNe Ia share similar continuum levels and spectral features, with the flux ratio being close to unity at both epochs and variations generally <50%, suggesting good agreement given differences in the line features. Considering that SNe 2011fe and 2018agk have similar evolutions of ejecta velocity as shown in Figure 6, similar $\Delta m_{15}$ and rise time (see Sections 3.2 and 3.4), and the similarity in their UV SEDs, we can qualitatively conclude that the progenitors of the two SNe Ia had similar metallicity.

### 3.2. Light Curve Fitting

We use the sncosmo package to fit Swope and DECam data with the SALT2 model.[58] For the Swope *B* and *u* bands, it is difficult to obtain as accurate a photometric calibration using the PS1 *griz* as for other bands, due to the lack of wavelength overlap and poor match of filter shape. Therefore we exclude the light curves for the Swope *B* and *u* bands from the SALT2 fit. When fitting, we fix parameters that are already determined via other methods: redshift, and Milky Way and host extinction. The results are listed in Table 1. The time of the peak in the *B* band is $\text{MJD}^B_{\text{peak}}$=58,204.178, ~0.2 days earlier than the Kepler maximum. The absolute peak magnitude in the *B* band is measured to be $M_B = -18.950 \pm 0.002$, and the decline rate in the *B* band is $\Delta m_{15} = 1.074 \pm 0.003$. All the photometric data are plotted in Figure 8, and part of the SALT2 light curve is plotted in Figure 9. All of SN 2018agk's SALT2 parameters are well within the range of a normal SN Ia, reinforcing that it is a typical normal SN Ia (Scolnic et al. 2018).

### 3.3. Kepler Photometric Calibration

Kepler features a broadband filter that covers the *g*, *r*, and *i* bands with a wavelength range of 4183.66–9050.23 Å. We calibrate the observed Kepler counts to physical AB magnitudes with the SN 2018agk spectra that fully cover the Kepler bandpass taken on MJD 58,194.45, 58,196.26, 58,201.26, and 58,229.17 (see Figure 9). Since there are few ground-based observations that coincide with the spectra, we normalize each spectrum by 'mangling' it to the SALT2 model *gri* magnitudes using the mangle_spectrum2 routine from the SNooPy package (Burns et al. 2011). We calculate the synthetic Kepler

---

[58] Due to the limited wavelength range, SALT2 cannot fit to the Kepler light curve of nearby SNe Ia within a certain redshift range, which includes SN 2018agk.
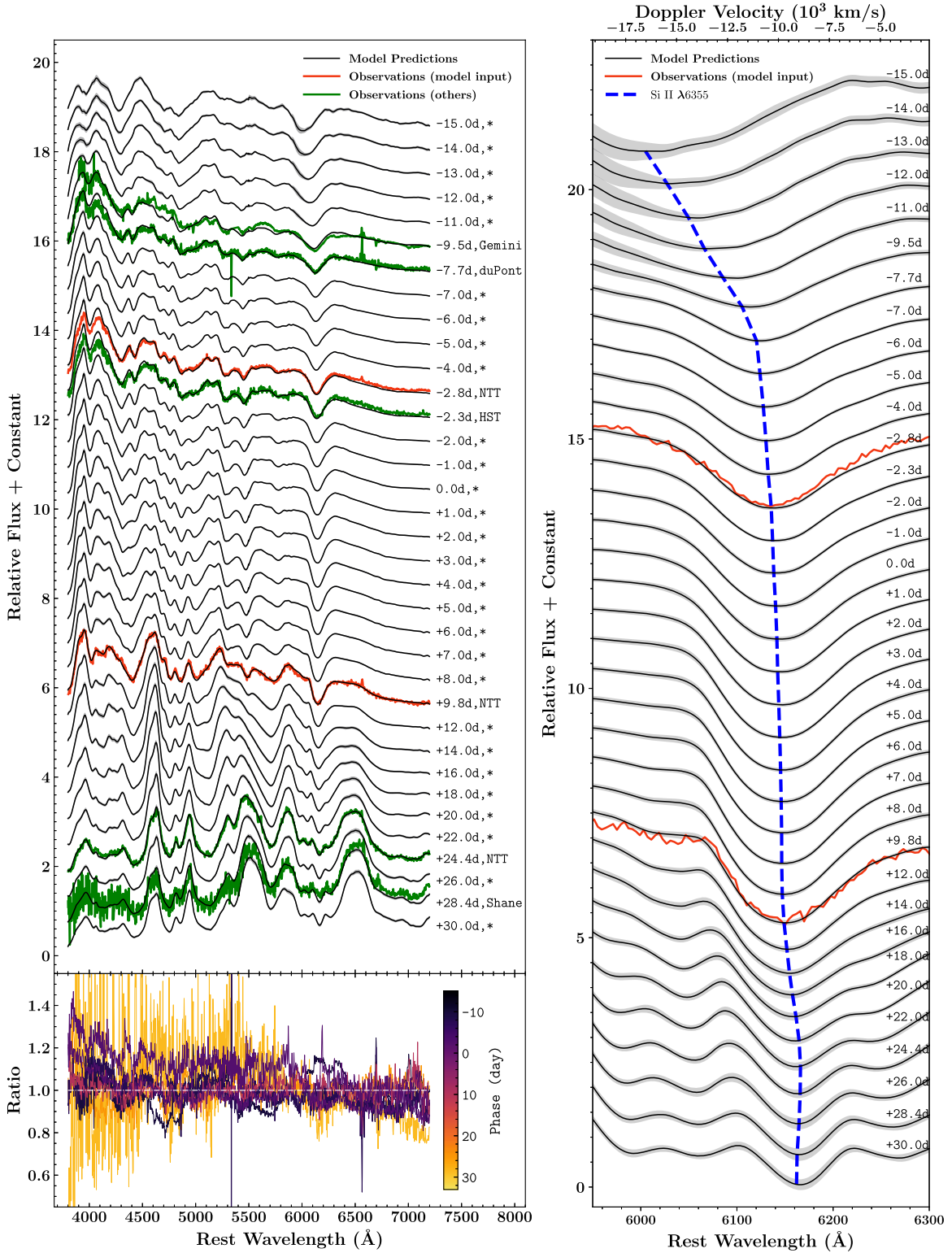
**Figure 5.** Left: the spectral sequence of SN 2018agk projected by the model based on Long Short-term Memory neural networks (Hu et al. in 2021). The two NTT spectra around the peak with the highest S/N (red) are used to build the projections (black), and the other high-S/N spectra (green) are included for a fidelity test. The gray regions indicate the $2\sigma$ standard deviation of the projection. All of the spectra have been shifted in the vertical direction and labeled with the corresponding phase and instrument. The bottom panel shows the ratios of the observations to the projections. The precision of the projections is around a few percent in general. Right: the evolution of Si II $\lambda6355$ of LSTM neural network projections of SN 2018agk. The blue dashed line indicates the trend of velocity evolution. For clarity, only two spectra used for building the projections are overplotted in red.

magnitude for each spectrum using the Kepler bandpass available on the Spanish Virtual Observatory (SVO) (Rodrigo et al. 2012; Rodrigo & Solano 2020) and algorithms in the `pysynphot` package (STScI Development Team 2013).

With the synthetic Kepler magnitudes, we then calculate the Kepler zero-point using the first three values from rise to peak. We limit the sample to these three points because at late times the Kepler data reduction method breaks down, leading to
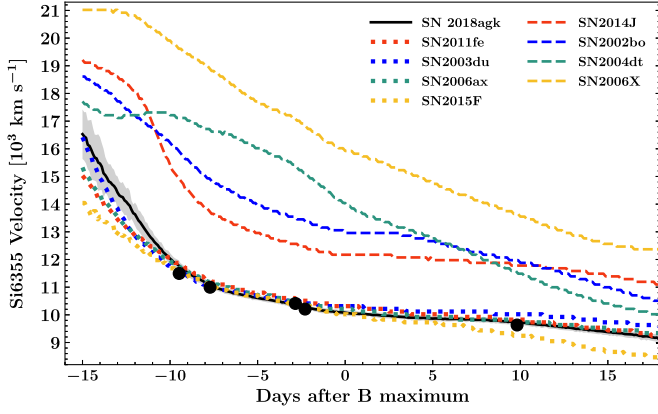
**Figure 6.** Evolution of the Si II λ6355 velocity of SN 2018agk. The black dots denote the direct measurements from the observations, and the black line and gray region denote the projections and uncertainty range from the model based on LSTM neural network presented in Hu et al. (in 2021). The evolutions of Si II velocity of normal SNe Ia (colored dotted lines) and high-velocity SNe Ia (colored dashed lines) projected from the same LSTM neural network have also been plotted for comparison.

unrealistic count levels (see Figure 9). To avoid biasing from residual sawtooth variability in the Kepler light curve we heavily smooth the light curve with the Savitzky–Golay smoothing method, using a third-order polynomial and a window size of 201 frames (100.5 hr). We calculate the zero-point according to

$$zp = Kp_{syn} + 2.5 \log(C), \tag{2}$$

where $Kp_{syn}$ is the synthetic Kepler magnitude and $C$ is the observed smoothed counts. We find all three points are consistent with $zp = 25.219 \pm 0.045$.

### 3.4. Modeling the Rise of the Light Curve

Kepler provided a single broadband light curve covering the pre-explosion and rising phase of SN 2018agk and starting from MJD 58,179.05. With these calibrated data, we determine the onset of the supernova light curve as follows: we define the interval from the start of Kepler observation to 22 days before $MJD_{max}^{K2}$ as the quiescent background and calculate the $3\sigma$ clipped weighted average and uncertainty $\sigma$ in this interval, and then we mark the time of K2 detection as the time when the GPR smoothed flux (see Section 2.2) rises to $1\sigma$ above the median flux of the background. We calculate $MJD_{det}^{K2}$=58,186.63 (17.14 days before $t_{Kepler}^{peak}$) as the result. In comparison, the first detection from ground was at $MJD = 58,186.29 \pm 0.02$ in the DECam $g$ band, ~0.3 days earlier than $MJD_{det}^{K2}$.

The early rise of our flux-calibrated light curve for SN 2018agk is shown in Figure 10. We also include the rise of SN 2018oh, which has a clear excess in the first ~5 days after first light (Shappee et al. 2018; Li et al. 2019; Dimitriadis et al. 2019a). The comparison shows that there is no large excess in SN 2018agk's Kepler light curve. We then use a series of different power-law models to fit the light curve of SN 2018agk. The form of the basic power-law model is defined as

$$f(t) = H(t_{fl})A(t - t_{fl})^{\alpha}, \tag{3}$$

where $A$ is the scale parameter, $t_{fl}$ is the time of the first light, and $H(t_{fl})$ is the Heaviside function such that $H(t_{fl}) = 0$ for $t < t_{fl}$ and $H(t_{fl}) = 1$ otherwise. We set the baseline flux equal to
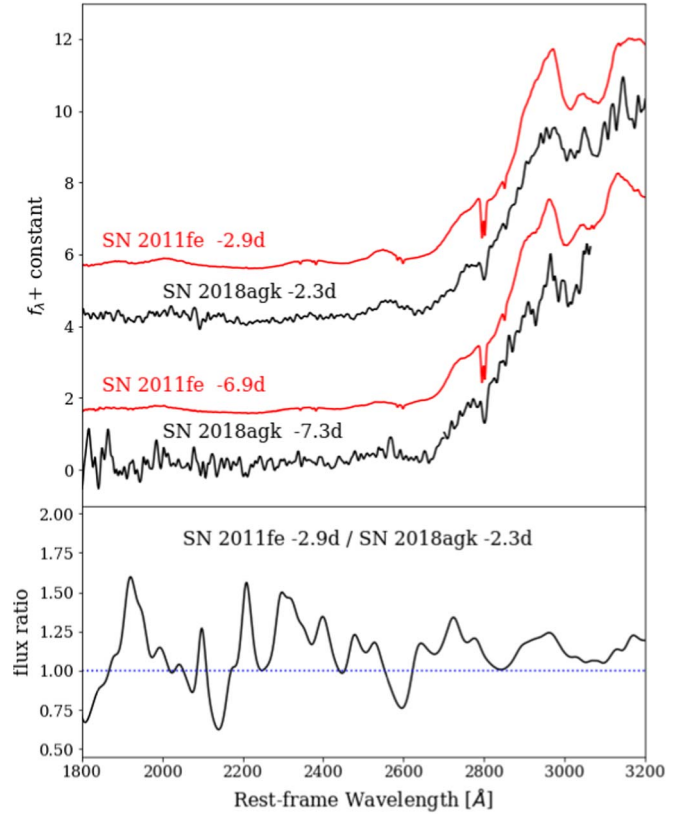


**Figure 7.** Top: HST UV spectra of SNe 2011fe (red) and 2018agk (black) at similar phases of around −2.5 days (top) and −7 days (bottom). The spectra have been dereddened and normalized to their flux around 3000 Å and also smoothed by a Gaussian filter with $\sigma = 1.5$ Å for presentation. Bottom: flux ratio of the ~−2.5 day UV spectra of SNe 2011fe and 2018agk normalized to their flux around 4000 Å. Due to the relatively low S/N in the UV region, the ratio has been smoothed by a Gaussian filter with $\sigma = 12$ Å for presentation.
(The data used to create this figure are available.)

0 in the fitting since the background flux has been subtracted out in normalization. We replicate the method used in Olling et al. (2015) and Dimitriadis et al. (2019a) and fit to data in the range from 25 days before peak until the Kepler flux reaches 35% of the peak flux (~MJD 58,193.18 or ~11 days before peak), using the Python package `scipy.optimize.least_squares`.

To test whether SN 2018agk follows the traditional "expanding fireball" model or a more general power-law rise, and to examine whether a bump feature exists in SN 2018agk, we fit the Kepler light curve with three models: a fixed single power-law, a $t^2$ rise leaving $t_{fl}$ as a free parameter, and two power laws with different $t_{fl}, t'_{fl}$ and $\alpha, \alpha'$. In order to judge the goodness of power-law fits with different numbers of parameters, we apply the Bayesian information criterion (BIC), which is a model selection technique based on the goodness of fit and number of model parameters. As presented in Priestley (1981), the BIC for a given fit can be calculated as

$$BIC = k \ln(n) + n \ln(\hat{\sigma}^2) \tag{4}$$

where $k$ is the number of parameters in the model, $n$ is the number of data points in the sample, and $\hat{\sigma}^2 = \chi^2/n$ is the variance, which is defined as the normalized mean of the
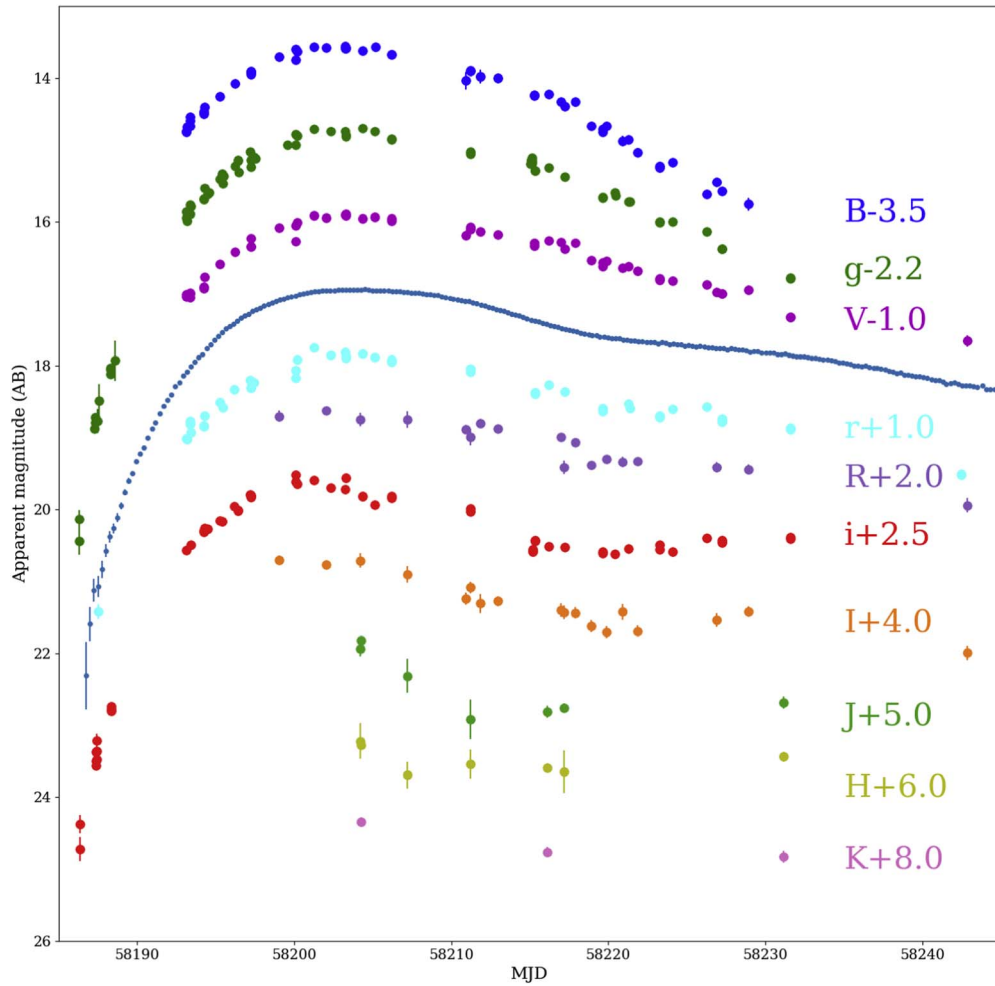
**Figure 8.** The optical and near-infrared light curves of SN 2018agk, including the 6 hr binned Kepler light curve. The light curves are shifted vertically for clarity of display.

**Table 1**
SALT2 Fitting Parameters

| $t_{\mathrm{peak}}^{B}$ | $x_0$ | $x_1$ | $c$ |
|---|---|---|---|
| $58,204.178 \pm 0.008$ | $(4.540 \pm 0.008) \times 10^{-3}$ | $0.220 \pm 0.015$ | $0.0168 \pm 0.0011$ |

squared differences between the data and the model. A model with smaller BIC is preferred in terms of balance between the agreement with data and the complexity of the model. Normally, a difference of >6 between BIC values indicates a statistically significant advantage.

The fitting results are listed in Table 2. The BIC of a single power-law fit is smaller than that of $t^2$ fit by >8 and thus is significantly preferable. Compared with the single power-law fit, a double power-law fit does not significantly improve the fitting quality, because $\chi^2$ of the two fittings are similar, and because its BIC is much larger as a result of a larger degree of freedom. Thus, we can conclude that the Kepler light curve of SN 2018agk can be well fitted by a single power law and there is no evidence of excess-like features at the earliest stage. The inferred time of first light is MJD 58,185.22, ~1 day before the first detection in DECam and Kepler as calculated in Section 3.2.

This result can be further validated when we compare the fit of SN 2018agk with that of SN 2018oh, as shown in Figure 10. For SN 2018oh we used the result of a two-component fit (power-law component for supernova flux and skewed Gaussian profile for excess) as described in Dimitriadis et al. (2019a). Comparing the residuals to the power-law fits shown in the lower panel makes it clear that the excess of SN 2018oh is well beyond the uncertainty limit of the binned light curve of SN 2018agk.

### 3.5. Color Evolution

Using the previous fits we calculate the range of color evolution for SN 2018agk. The results in the crucial early phase (~10 days after $t_{\mathrm{fl}}$) are plotted in Figure 11, along with DECam and Swope measurements in both $g$ and $i$ bands made $\lesssim 4$ days and $\gtrsim 7$ days relative to $t_{\mathrm{fl}}$ respectively. Overall, the color of SN 2018agk in these three bands is relatively constant in the first ~10 days, with variance <0.1 mag, excluding the first observation due to the large uncertainty in the $g - i$ band. A linear fit to $g - i$ of SN 2018agk gives a rate of change of $0.007 \pm 0.003$ mag day$^{-1}$. Qualitatively speaking, this result agrees with the assumption of the fireball model that the
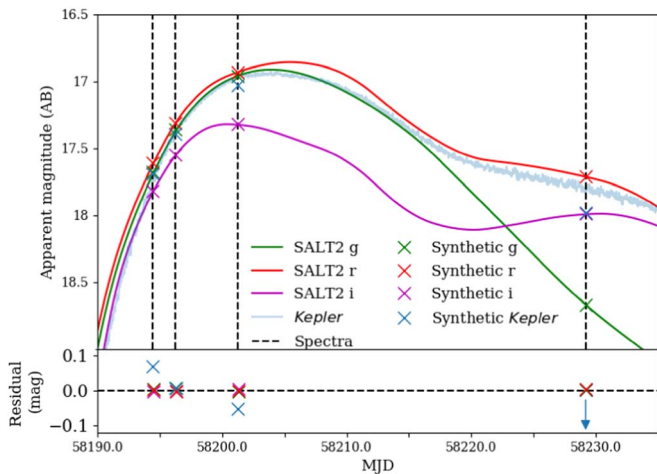
**Figure 9.** Calibration of Kepler photometric zero-point with synthetic magnitudes and SALT2 fitting results. The black dashed lines mark the time of spectra used to calculate the synthetic magnitude, and colored lines are the fitted SALT2 model in *gri* bands, as described in Section 3.2. Spectra used to generate synthetic magnitudes are calibrated to the SALT2 model, from which the Kepler zero-point $zp$ is obtained. The large offset ($\sim$0.2 mag) of observed and synthetic Kepler magnitudes around MJD $\approx$ 58,229.2 indicates the breakdown of the Kepler data reduction method at late times. Parameters from SALT2 fitting are listed in Table 1.

temperature of the photosphere remains approximately constant when it expands.

We also compare SN 2018agk with other SNe Ia that have early photometric measurements or series of spectra. Our sample includes SN2011fe (Pereira et al. 2013), SN 2015F (Cartier et al. 2017), iPTF16abc (Miller et al. 2018), SN 2017cbv (Hosseinzadeh et al. 2017), SN 2018gv (Miller et al. 2020), and SN 2018oh (Shappee et al. 2018; Li et al. 2019; Dimitriadis et al. 2019a). In this sample, SN 2011fe, SN 2015F, and SN 2018gv are well-observed normal SNe Ia, whereas SN 2017cbv and SN 2018oh are among few SNe Ia that have been detected with significant excess flux at early times ($\lesssim$5 days after time of first light), and iPTF16abc has a nearly linear rise in the *g* band with a relatively limited amount of data. SN 2018gv has photometric data in the *g'* and *i'* bands from the Sinistro camera at the Las Cumbres Observatory from very early phases. SN 2018oh has measurements in *g* and *i* from Pan-STARRS within the first day after explosion, but due to the large uncertainty ($\gtrsim$0.3 mag) we do not include them in the comparison. SN 2011fe lacks *i*-band data, but Pereira et al. (2013) has produced a spectrophotometric time series with high precision, which enables us to calculate synthetic photometry in the *g*, *i*, and Kepler bands. SN 2017cbv has both photometric measurements and spectra in the early phase. The synthetic photometry of SN 2011fe and SN 2017cbv in the *g*, *i*, and Kepler bands is calculated through the same routine used in Section 3.3.

## 4. Discussion

In the traditional "expanding fireball" model, the photospheric temperature and expansion velocity remain constant for several days after explosion, and thus an SN Ia light curve follows $L \propto t^2$ as ejecta expand in all bandpasses (Arnett 1982). Observations suggests that light curves of different SNe Ia may follow a power law $L \propto t^\alpha$ with some distribution of index $\alpha$ centered on 2 (e.g., Hayden et al. 2010; González-Gaitán et al. 2012; Miller et al. 2020). The rise of SN 2018agk's light curve

is well described by a single power law with $\alpha = 2.25 \pm 0.07$ (see Table 2), in good agreement with the other SNe Ia from the Kepler prime mission (Olling et al. 2015) and the ground-based samples. With the excellent cadence and high S/N of SN 2018agk's Kepler light curve, we can put strong constraints on the existence of excess flux, and we can also determine the time of first light to a very high precision. Combined with the 1 day cadence DECam observations in the first four days after first light, we find that that there is no significant color evolution in the first $\sim$10 days after explosion.

Clues to the progenitor systems can be found through early observations of SN Ia light curves soon after explosion. Different mechanisms have been proposed to create early excess features with different characteristics in SN Ia light curves, e.g., Kasen (2009) shows that in the SD model, the interaction between SN ejecta and a nondegenerate companion can produce a blue excess on top of the normal SN Ia flux in light curves within days after explosion. Such early bump features have only been detected in a very limited number of normal SNe Ia. For both SN 2017cbv and SN 2018oh, interaction with a subgiant companion can reproduce the early optical light curve within the uncertainty range, but the late-time spectra lack H and He features predicted by this model (Hosseinzadeh et al. 2017; Dimitriadis et al. 2019b). Levanon & Soker (2019) further compared the three processes for the early light excess of SN 2018oh and argue that the interaction of ejecta with disk-originated matter in the DD scenario accounts for the early excess better than interaction with a companion or the presence of $^{56}$Ni in the outer ejecta. Nonetheless, the uncertainty in the underlying supernova flux in different bands at the earliest stage strongly degrades the information that can be interpreted from the model fitting. Early multiband observations on SNe Ia with clearly no early excess features are crucial for future studies.

### 4.1. Color Evolution of SNe Ia with and without Early Excess Flux

The color evolution in the earliest phase of SNe Ia can be a crucial piece of evidence in distinguishing different progenitor models, as discussed above. Still, the small sample of high-quality measurements in this critical time window limits the application of such studies. Currently, there are not enough SNe Ia light curves with sufficient cadence and S/N at these early epochs to build a reliable SN Ia template.[59]

To reveal the prototypical color evolution of normal SNe Ia without excess flux and distinguish them from those with excess flux, we show the color evolution of SNe Ia with early observations in Figure 11. In general, the normal SNe Ia without early excess in our sample (SN 2011fe, SN 2015F, SN 2018gv, and SN 2018agk) have similar colors, with only a small color evolution toward the blue. In $g - i$, the color changes less than $\sim$0.2 mag in the first 10 days. Remarkably, there is a clear distinction between normal SNe Ia and SN 2017cbv in $g - i$, where the latter is significantly blue not only during the time of excess, but up to 10 days after first light. In addition, the synthetic colors of SN 2017cbv ($g -$ Kepler and Kepler $- i$) show a similar trend to $g - i$; they are bluer than SN 2011fe. On the other hand, iPTF16abc (with a

---

[59] There do exist templates at the earliest stage, e.g., SiFTO (Conley et al. 2008), though the uncertainties are very large due to the small number of objects.
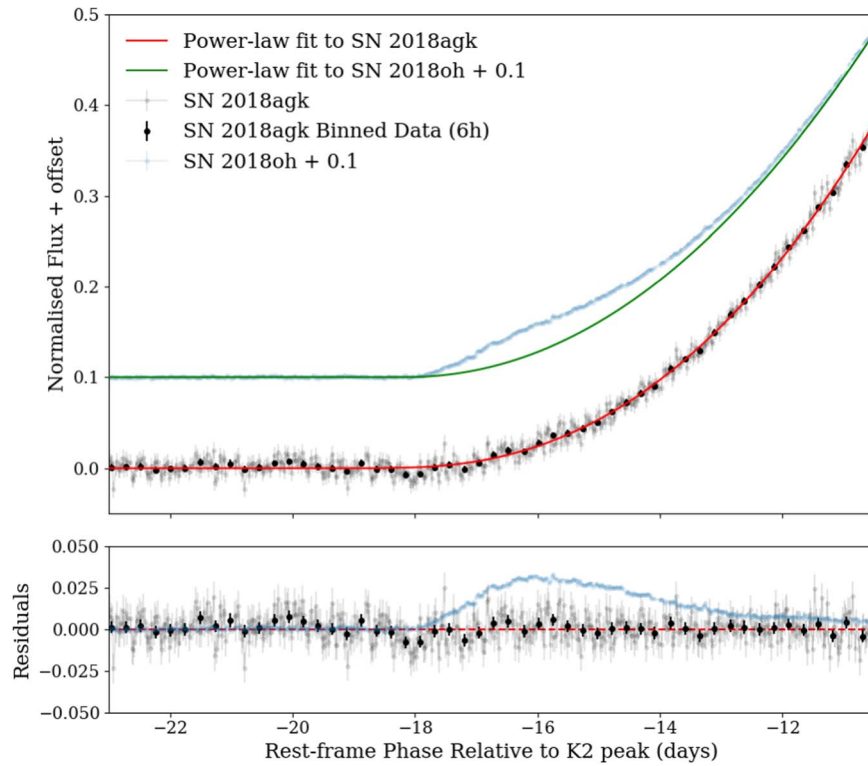
**Figure 10.** Top: comparison between the early rise and power-law fits for SNe 2018agk and 2018oh. Phases are relative to the time of peak brightness in the Kepler band, and light curves have been normalized by their peak magnitudes. The raw Kepler light curves of SNe 2018agk and 2018oh with 30 minutes cadence are plotted as gray and blue points respectively. The 6 hr average for SN 2018agk is shown as black points, and the power-law fits for SNe 2018agk and 2018oh are shown as red and green lines, respectively. For SN 2018oh, we used the power-law parameters from the two-component fit (power law + skewed Gaussian) described in Dimitriadis et al. (2019a). Bottom: residuals of the SN 2018agk fit compared with the excess of SN 2018oh relative to its power-law component in the fit. SN 2018agk is well fit by the power-law rise without excess flux, whereas the excess is clear for SN 2018oh. For clarity, the $t^2$ and double power-law fits to SN 2018agk are not included because they are almost indistinguishable from the single power-law fit in most regions.

**Table 2**
Different Results of Power-law Fitting to the Kepler Light Curve of SN 2018agk

| Model | $t_{\rm fl}$ | $t_{\rm fl}'$ | $\alpha$ | $\alpha'$ | $A\ (\times 10^3)$ | $A'\ (\times 10^3)$ | $f_0\ (\times 10^4)$ | $\chi^2$ | BIC |
|---|---|---|---|---|---|---|---|---|---|
| $t^2$ rise | $-17.53 \pm 0.03$ | ... | 2 | ... | $6.79 \pm 0.03$ | ... | $-3.2 \pm 4.2$ | 497.0 | $-3880.5$ |
| $t^\alpha$ rise | $-18.09 \pm 0.16$ | ... | $2.25 \pm 0.07$ | ... | $3.53 \pm 0.06$ | ... | $-7.6 \pm 4.3$ | 478.5 | $-3896.7$ |
| Double $t^\alpha$ rise | $-14.94 \pm 0.31$ | $-17.05 \pm 0.18$ | $1.79 \pm 0.11$ | $1.14 \pm 0.20$ | $11.4 \pm 2.8$ | $20.3 \pm 4.6$ | $-7.3 \pm 4.1$ | 462.6 | 2257.3 |

linear rise in the $g$ band) seems to have a similar $g - i$ color curve to normal SNe Ia without excess. However, iPTF16abc shows very different behavior in $B - V$ color (Stritzinger et al. 2018) and will be discussed later in more detail. Notably, in Kepler $- i$, the earliest high-S/N photometric measurement of SN 2018oh at $t \sim 1$ day after first light is significantly bluer than those of SN 2018agk, while the synthetic colors of SN 2011fe and SN 2017cbv (empty symbols in Figure 11) have a smaller difference in the earliest stage in this band.

This result is slightly different from previous studies in other optical bands. Previous statistical study on the SNe Ia sample from the Zwicky Transient Facility in $g$ and $i$ bands found relative homogeneity in early color ($g - i \sim 0.15$ mag), along with a large scatter of color slope in $g - r$ for individual events (Bulla et al. 2020; Miller et al. 2020). Stritzinger et al. (2018) analyzed a sample of 13 SNe Ia with early measurements in $B$ and $V$ bands, and found two populations with different color evolution in $B - V$ within the first $\sim 3$ days after explosion (see Figure 2 in Stritzinger et al. 2018). The "early red" group has

redder initial color and turns blue rapidly in $B - V$, at a rate of $\sim 0.5$ mag in the first 10 days, and has a typical luminosity and decline rate among SNe Ia. The "early blue" group is $\sim 0.5$ mag bluer than the "early red" group in $B - V$, evolves at a negligible rate, and tends to be brighter than the red group. Spectroscopically, the SNe Ia in the "early blue" group tend to have weaker Si II absorption features and lie within or close to the shallow silicon (SS) subtype in the Branch diagram (see Figure 4), while the SNe Ia in the "early red" group belong to either core normal (CN) or cool (CL) type. Qualitatively speaking, the spectral features of SN 2018agk fit into the CN class (see Section 3.1), and it has an intermediate peak brightness and decline rate among the normal SNe Ia sample. Combining all the characteristics, SN 2018agk aligns with the "early red" events as characterized in Stritzinger et al. (2018). In terms of early color, in $g - i$ the SNe Ia in the "early red" group (SN 2011fe, SN 2015F, and SN 2018agk) are similar to iPTF16abc but are significantly redder than SN 2017cbv, both of which belong to the "early blue" group. Meanwhile, all the
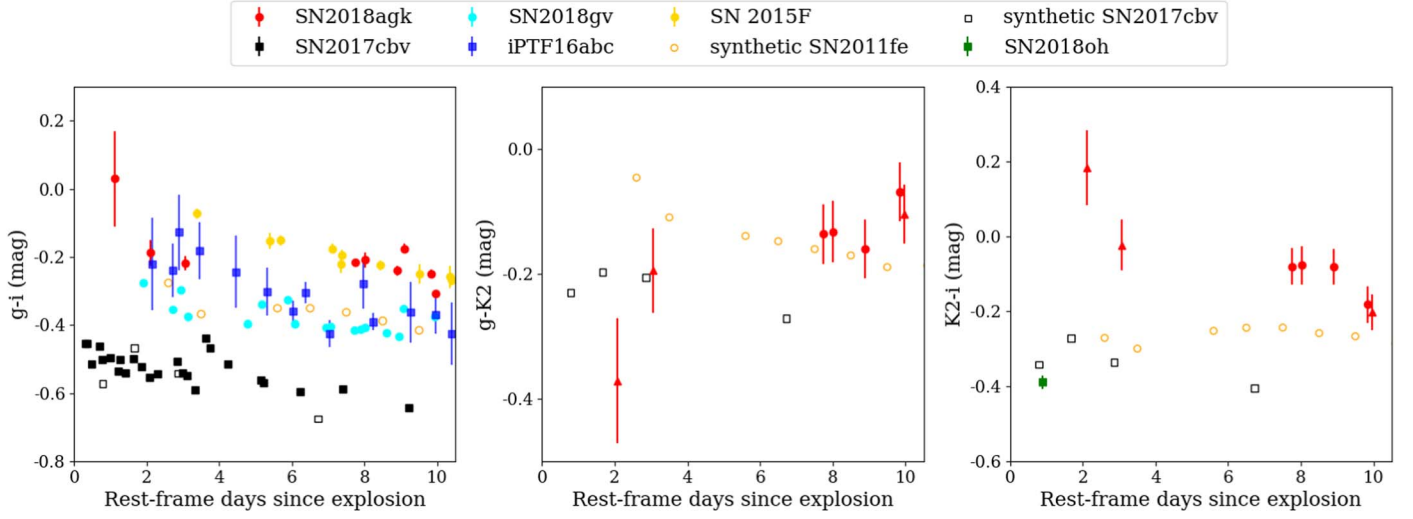
**Figure 11.** Color evolution of SN 2018agk in $g - i$ (left), $g - $ Kepler (middle), and Kepler $- i$ (right). We also include other SNe Ia with early observations, such as photometric measurements of SN 2015F, SN 2017cbv, SN 2018oh, and SN 2018gv (in $g$ and $i$ bands), alongside synthetic magnitudes of SN2011fe and SN 2017cbv calculated from photometrically calibrated spectra. All photometric measurements include uncertainties, but they may be too small to be seen. The SNe Ia without a bump and iPTF16abc are concentrated in the $g - i$ band within the range $-0.2 \pm 0.2$, while SN 2017cbv is bluer than this normal SNe Ia group. All SNe Ia in our sample have relatively stable color evolution in the first $\sim$10 days.
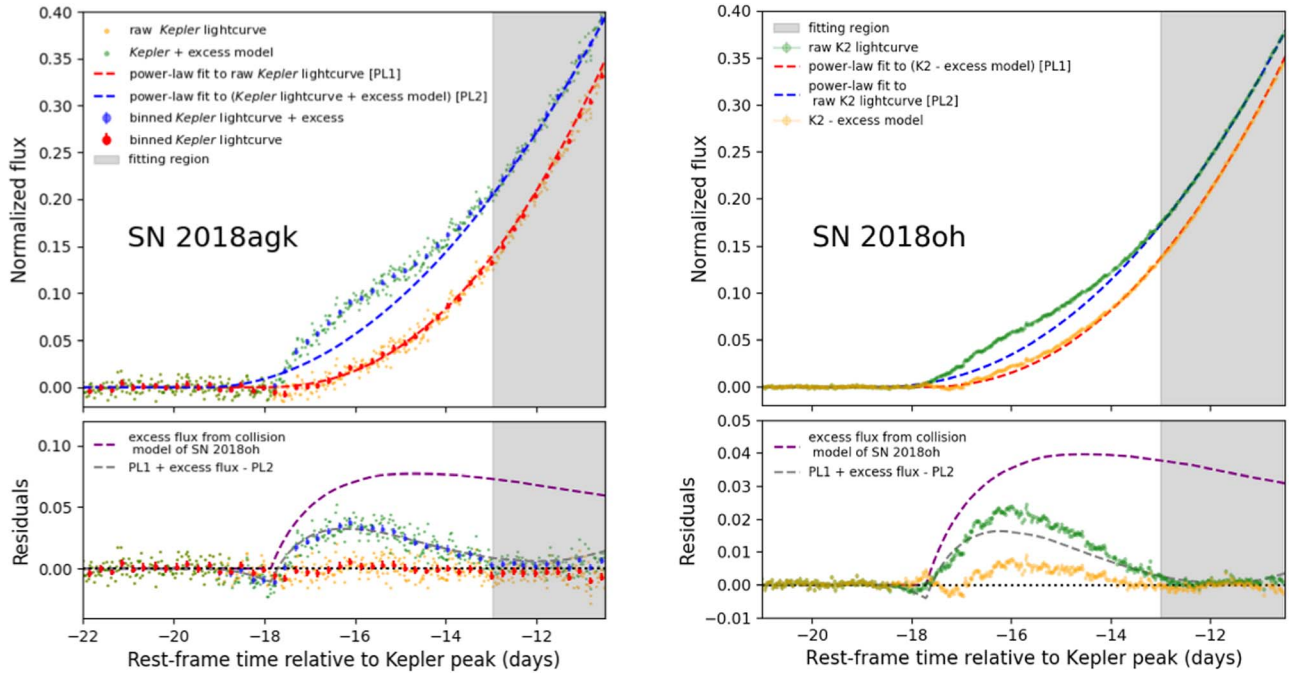


**Figure 12.** Left: the top panel shows a power-law fit to the original Kepler light curve of SN 2018agk (PL1, red) and the Kepler light curve plus long-tail excess from the companion-interaction model (PL2, blue). The bottom panel shows the residuals relative to each power-law fit. The excess model (purple) is also included for comparison in the bottom panel. The gray line represents the difference between PL1 plus the excess model and PL2. With the traditional power-law fit method for excess detection, the excess can be strongly underestimated, as can be seen by comparing the purple and gray dashed lines. The excess model comes from the fit to the bump of SN 2018oh and is added to SN 2018agk in physical units before being normalized to the peak of SN 2018agk. We note that the small dip at $\sim$−18 days comes from the difference in $t_0$ of two power-law fittings. Right: same comparison between the raw light curve of SN 2018oh in Kepler (green and blue) and the light curve with excess model subtracted (yellow and red).

SNe Ia in our sample evolve at a slow rate of no more than $\sim$0.02 mag per day in the first 10 days in $g - i$, and the rapid drop of the "early red" group in $B - V$ is not seen.

Foley et al. (2012) analyzed SN 2009ig, an SN Ia discovered hours after explosion with significant $B - V$ color evolution at early times. The redder colors (e.g., $V - R$ and $R - I$) of SN 2009ig do not evolve quickly, indicating that the rapid change in $B - V$ color is not caused by a change in the broad wavelength continuum. Instead, the early spectra of SN 2009ig during this period show an Si II 4000 Å feature that is so blueshifted and broad that it merges with the Ca H and K absorption feature. As a result, the flux at 4000 Å is severely

13
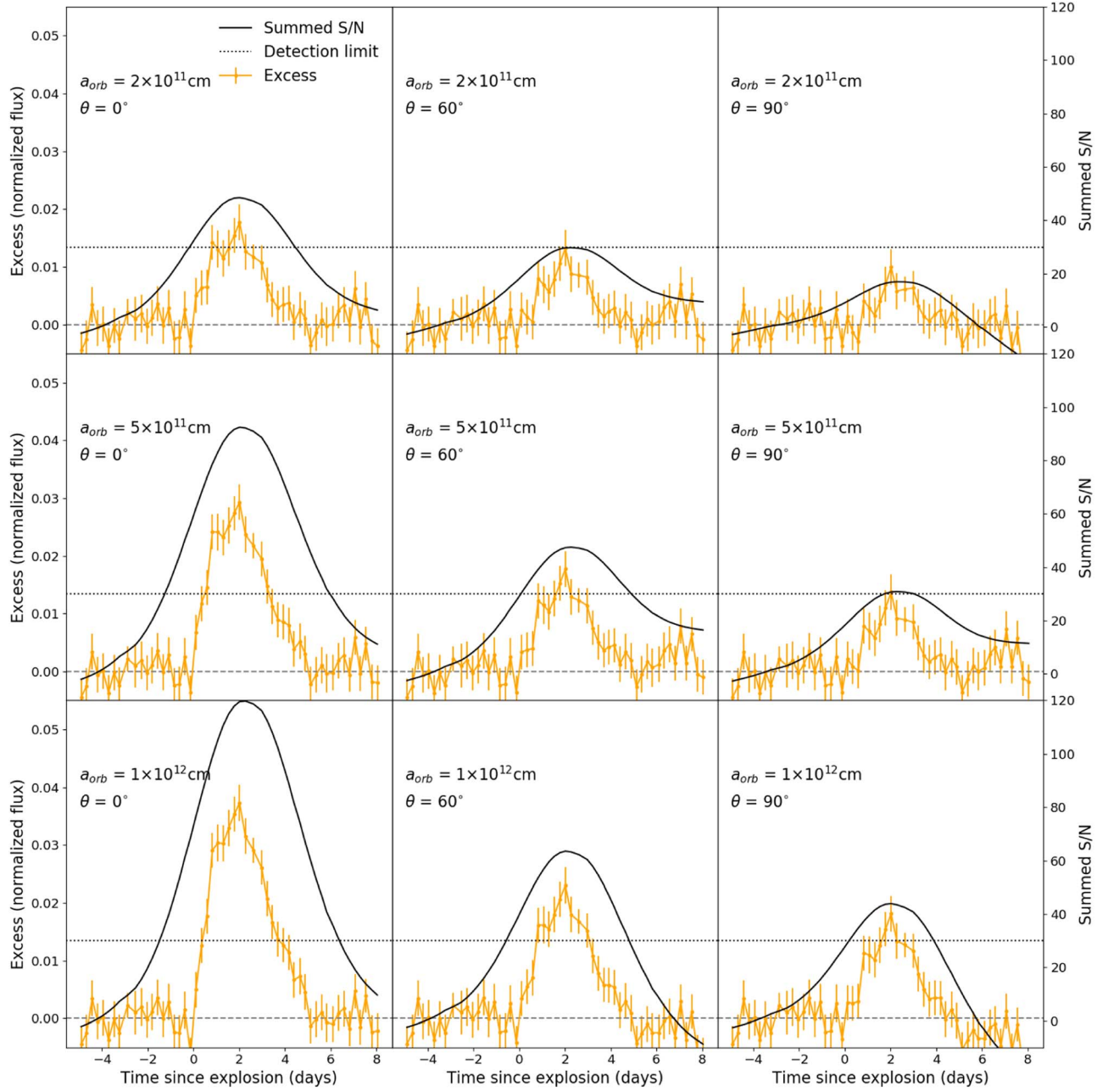
**Figure 13.** The excess relative to the power-law fit of the light curve from the companion-interaction model with different parameters, calculated in the same way as shown in Figure 12. The Kepler light curve of SN 2018agk is used to approximate the supernova flux in the model. The power law is fitted on the time interval starting from 6.5 days to 8 days after explosion. The black curves are the rolling sum of S/N with a Gaussian window. We conservatively set the detection limit of excess as S/N = 30, marked as the black horizontal dotted line.

depressed. Over the next few days, corresponding to the time of rapid $B - V$ color evolution, the features become distinct and more similar to the appearance of SN Ia spectra near peak brightness. This strongly indicates that spectral features likely drive these color changes. Such a mechanism may explain the difference in color evolution in different bands seen for the full sample, although a larger and more complete sample of SNe Ia will be necessary to resolve this issue.

In general, different models give qualitatively different predictions on the early color excess in SNe Ia. Overall the comparison between the normal SNe Ia sample with SN 2017cbv agrees with fits from the companion-interaction model in Hosseinzadeh et al. (2017) and simulations of the $^{56}$Ni shell model from Magee & Maguire (2020), both of which can

produce a bluer color than the fiducial model without a bump. Still, the exact prediction may vary with different model parameters, e.g., the fit to SN 2018oh has a redder color $\sim$3–8 days after explosion than SN 2017cbv in Magee et al. (2021). Uncertainties in the fiducial models at the early time also limit our ability to fit models with high fidelity (e.g., see the discussion in Magee et al. 2021).

$t_{\rm fl}$ of SNe Ia in our sample likely faces systematic uncertainties. They are inferred based on the $t^{\alpha}$ fit with slightly different schemes in separate papers, with varying lengths of the dark phase. Nonetheless, as shown in Figure 11, SNe Ia in our sample only have a very low level of variability in color at the early time. Therefore, the uncertainty in $t_{\rm fl}$ should not have a big influence on our conclusion.
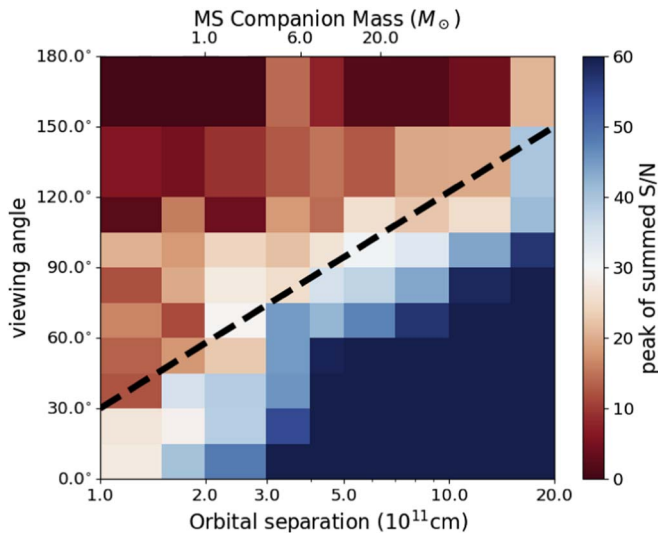
**Figure 14.** The peak of rolling summed S/N with a Gaussian window for the companion-interaction model with different orbital separations $a_{orb}$ and viewing angles $\theta$, as introduced in Figure 13. We empirically set the detection limit to be S/N $\approx 30$, corresponding to the white blocks in the color map; the blue region represents the detectable excess, while in the red region the excess is undetectable. The black dashed line qualitatively marks the bounds of detectability of excess in parameter space. The mass of a main-sequence companion in a WD–MS binary system undergoing Roche lobe filling with a certain orbital separation is labeled at the top.

### 4.2. Detectability of a Prominent Bump in SN 2018agk

High-cadence surveys including those by Kepler and the Transiting Exoplanet Survey Satellite (TESS) probe a large sample of SNe Ia soon after their explosion, making it possible to study the early light curve of SNe Ia statistically and estimate the fraction of SNe Ia with detectable early excess features. Resolving the detectability of the early excess and potential contamination will be a key component to such studies. Considering the current limitation in fitting with physical models, algorithms to detect model-independent excess are necessary for searching for abnormal features in the rise of SNe Ia. In this section we present the application of the rolling sum algorithm to evaluate excess flux in early SNe Ia light curves.

With the high-quality light curve of SN 2018agk, we try to evaluate the factors influencing efficiency and accuracy of bump detection quantitatively. We add the excess model onto SN 2018agk's light curve and evaluate the significance of bump detection with the method described in Dimitriadis et al. (2019a), which fits a power law to a time interval well after the explosion as the baseline light curve and finds the excess signal in the residual in the days after explosion. We use an excess flux model based on a companion-interaction model fitted to SN 2018oh in Dimitriadis et al. (2019a), with a subgiant companion at a separation of $2 \times 10^{12}$ cm, assuming the supernova ejecta has a mass of $1.4\,M_{\odot}$ and velocity of $8 \times 10^{8}$ cm s$^{-1}$. With the assumption that the luminosity of the bump has a weak dependence on supernova luminosity, we add the excess in physical units before normalizing to the peak of SN 2018agk.

To minimize the degeneracy issue and consequent large uncertainty in power-law fitting, we perform the Markov Chain Monte Carlo (MCMC) fitting with the `emcee` package (Foreman-Mackey et al. 2013) assuming a Gaussian prior

distribution for $t_0$ and $n$ and a flat prior distribution for scale factor $A$. The mean and standard deviation of $t_{fl}$ are set to be $18.7 \pm 1.8$ days as estimated from Miller et al. (2020), and we use a power-law index in the $r$ band $n_r = 2.0 \pm 0.5$ to simulate the distribution of $n$ in the Kepler bandpass, considering the similar effective wavelengths of the Kepler and $r$ bands.

The left panel of Figure 12 shows the power-law fit to the Kepler light curve of SN 2018agk (PL1) and the same light curve plus the excess flux model (PL2), along with the residuals of these two power-law fittings. In the right panel of Figure 12 we show the fitting with the same setting on SN 2018oh, with or without the excess flux model subtracted. All of the fits are done in the window of 13–10.5 days before $t_{peak}^{K2}$. One noticeable difference is that in both fits $t_0$ inferred from light curves with excess is $\sim 1.5$ days earlier than $t_0$ inferred from the original light curve. In the residual plot, we show the contrast between the excess model (purple dashed line) and the reconstructed bump after power-law fitting. Clearly, due to the extended tail of collision flux, the power-law fit overestimates the supernova flux and underestimates the excess flux by a large amount after subtraction. This is an indication of the low effectiveness of current routines to detect excess. This problem will be exacerbated for ground-based surveys with much larger cadences or similar space telescopes with shallower detection limits (e.g., TESS). Therefore, establishing a robust fiducial model for early light curves of SNe Ia without excess is necessary for future searches for early excess. Meanwhile, signatures in either early spectra or color evolution, as analyzed previously, would also be key evidence to facilitate bump detection and distinguish different models.

### 4.3. Constraints on the Progenitor System in the Case of the SD Model

We adapt the fitting scheme from Section 4.2 to give a qualitative estimate of the detectability of the bump and constrain the potential progenitor system for SN 2018agk in the case of the SD model. We use the analytic companion-interaction model (Kasen 2009) multiplied by an angular dependence term calculated in Brown et al. (2012) as a test case. We first add excess flux to its Kepler flux, and then fit a power law to a relatively late time interval with MCMC and estimate the detectability of excess in residuals within $\sim 5$ days after explosion. The excess flux is mainly determined by four parameters: the orbital separation of the binary $a_{orb}$, the viewing angle $\theta$, the velocity $v$, and the mass $m_{ejecta}$ of the ejecta. While $\alpha$ and $\theta$ can vary over relatively large ranges, $v$ and $m_{ejecta}$ are usually well constrained for typical SNe Ia in the SD model. We set $v = 8 \times 10^{8}$ cm s$^{-1}$ and $m_{ejecta} = 1.4\,M_{\odot}$ in accordance with a typical SNe Ia explosion with kinetic energy of $10^{51}$ erg, and we focus on the effect of a different viewing angle and orbital separation.

To evaluate the overall signal of excess on top of the power-law rise, we applied the rolling method with a Gaussian window to sum the signal-to-noise ratio of the "detected excess" over its extended duration. Considering that the typical duration of the detected bump is $\sim 5$ days, we use a Gaussian with $\sigma = 2$ days over a 12 day window, and then we normalize the results to the rolling sum of a constant background to remove the edge effect in the algorithm. The left column of Figure 13 shows a set of examples with $\theta = 0°$ and different orbital separations $a_{orb}$ and the top column shows results for fixed $a_{orb} = 2 \times 10^{11}$ cm at different viewing angles. As can be seen from the plot, this method can effectively take the

accumulated signal in an extended interval into account and smooth out the random noise in the light curve at the same time. We conservatively set the detection limit as $S/N \approx 30$ as the dotted line in Figure 13, which is well above the rolling sum of baseline $S/N$ without excess, i.e., the model with viewing angle $\theta = 180°$. We run the same algorithm on excess for a large set of different $\theta$ and $a$ and plot the color map of the peak of summed $S/N$ with regard to these two parameters in Figure 14. The blue and red regions represent the regions of detectable and undetectable excess in the parameter space, and we add a black dashed line to mark the approximate detection limit for the SD progenitor system of SN 2018agk in Figure 14

We are able to set a rough constraint on the potential progenitor system of SN 2018agk in the SD model and the detectability of excess for similar events with high-cadence light curves. An assumption of the companion-interaction model is that the companion overfills its Roche lobe, and the orbital separation $a$ is correlated with the companion radius $R$ and the mass ratio of the binary $q$, approximately following the equation (Eggleton 1983)

$$a_{\mathrm{orb}} = \frac{0.6q^{2/3} + \ln(1 + q^{1/3})}{0.49q^{2/3}} R. \qquad (5)$$

For simplicity we estimate a typical main-sequence (MS) star in a WD–MS binary with mass ranging from 1 to 20 $M_\odot$ and mark the mass corresponding to certain $a_{\mathrm{orb}}$ at the top of Figure 14, though such binary systems are believed to likely produce less energetic explosions, e.g., nova (Prialnik & Shara 1986; Shara et al. 1986; Michaely & Shara 2021). In the more favorable SD models, the companions are usually believed to be subgiants or red giants (Branch et al. 1995; Hachisu et al. 1996; Wang et al. 2010). Such a binary system will have larger $a_{\mathrm{orb}}$ for the same mass range, and thus will only be more constrained than the WD–MS system analyzed here. As shown in Figure 14, a WD–MS binary progenitor system with viewing angle $\theta \lesssim 60°$ will produce a prominent excess that is detectable by our rolling algorithm for a typical SN Ia such as SN 2018agk in Kepler. When $\theta$ increases to $\gtrsim 120°$, the excess becomes undetectable for such WD–MS binary systems. From this perspective, viewing angle seems to be the more dominant factor in the detectability of the bump, and a statistical analysis of SNe Ia with high-cadence early light curves from Kepler and TESS will be the key to determining whether SD systems can be a major channel for SNe Ia or not.

## 5. Conclusions

In this paper, we report and analyze the photometric and spectroscopic observations of SN 2018agk, a normal SNe Ia that occurred within the Kepler Campaign 17 field. The SN has an exquisite high-cadence Kepler light curve, showing no early excess flux beyond a power-law rise. Combined with ground-based photometry in multiple bands, especially the 1 day cadence DECam observations within the first $\sim$4 days after first light in Kepler, we are able to determine the color evolution of a prototypical SNe Ia without excess flux in the earliest stages.

1. The spectra of SN 2018agk match the features of a Branch-normal SN Ia without peculiarity, e.g., the pEW and velocity of Si II fit in the range of normal SNe Ia. In particular, the HST UV spectrum near peak shows

similarities in continuum levels and line features with SN 2011fe, indicating similar progenitor metallicity of the two SNe Ia.

2. The early Kepler light curve shows a clear power-law rise. Using a BIC test, we find that a single power law with an index of $\alpha = 2.25 \pm 0.07$ fits the data better than a canonical fireball model ($L \propto t^2$) or a double power-law fit. There is no evidence of early excess flux in the fit.

3. Combined with DECam $g$ and $i$ observations in the first $\sim$4 days after first light in Kepler, we calculate the early color evolution and compare it with other SNe Ia with and without early excess flux. We show that the normal SNe Ia without bumps have similar color in the first $\sim$10 days after first light. Of the SNe Ia with bumps, SN 2017cbv has a bluer color during this period, especially in $g - i$, but SN 2015F has a similar color to other normal SNe Ia. All SNe Ia in our sample have very low levels of variability in color during this early rise phase ($|\Delta(g - i)/\Delta t| \lesssim 0.02$ mag day$^{-1}$), in contrast to the steep evolution in $g - r$ for a large portion of SNe Ia in Bulla et al. (2020), and the rapid drop in $B - V$ for some "early red" SNe Ia as found in Stritzinger et al. (2018). Qualitatively speaking, this result agrees with the predictions by both the companion-interaction model and the $^{56}$Ni shell model, but a larger sample and simulations with higher precision are necessary to further differentiate between these progenitor channels.

4. We examine the efficiency in bump detection by adding the excess model derived from a fit to SN 2018oh to the Kepler light curve of SN 2018agk, and applying the detection algorithm from Dimitriadis et al. (2019a). With an extended tail into $\gtrsim 5$ days after explosion, the excess can strongly influence the power-law fitting results, shifting $t_{\mathrm{fl}}$ by $\sim$1 day even in fitting with a strong prior distribution, and the "bump" can be significantly underestimated. Thus, a thorough analysis of the efficiency and contamination of bump detection will be needed for future studies.

5. We further test the detectability of bumps in the companion-interaction model and constrain the physical properties of a possible SD progenitor with the rolling sum method. We found that in the case of SN 2018agk, an MS or more evolved companion (e.g., subgiant or red giant) with mass larger than 1 $M_\odot$ and viewing angle smaller than 60° can be ruled out, while the excess from a WD–MS system with viewing angle larger than 120° is still below the detection limit. On the other hand, the influence of MS companion mass on the detectability of excess is relatively low. A statistical analysis of the SNe Ia sample from Kepler and TESS will be the key to revealing whether SD progenitor systems are the main channel for SNe Ia or not.

Overall, SN 2018agk has no signatures of spectroscopic and photometric peculiarities. Its early Kepler light curve closely follows a power-law rise and has no signature of excess flux, and early DECam observations show no early color evolution of this event. Thus, SN 2018agk can serve as a prototype for normal SNe Ia without early excess for future studies on searching for early excess.

While it is difficult to exclude any progenitor system for SN 2018agk alone, a statistical study on the SNe Ia sample

with a high-cadence light curve from Kepler and TESS will be a brand new window to shed light on the progenitor systems of SNe Ia. To facilitate such an investigation, a complete statistical study on the detectability of early excess in different models will be crucial.

*Facilities:* Kepler, HET, Gemini:Gillett, SSO:1 m, Du Pont, NTT, FTN, Shane, Keck:I, SOAR, Blanco, Swope, CTIO:1.3 m, PS1.

*Software:* Astropy (Astropy Collaboration et al. 2018), IRAF (Tody 1993), SAOImage DS9 (Smithsonian Astrophysical Observatory 2000), sncsomo (Barbary et al. 2016), Matplotlib (Hunter 2007), SciPy (Virtanen et al. 2020), NumPy (Harris et al. 2020), emcee (Foreman-Mackey et al. 2013), celerite (Foreman-Mackey et al. 2017), corner (Foreman-Mackey 2016), extinction (Barbary 2016), pysynphot (STScI Development Team 2013), swarp (Bertin et al. 2002), Dophot (Schechter et al. 1993), HOTPANTS (Becker 2015).

## Appendix

Tables of spectroscopic observations and ground-base photometric observations.

**Table 3**
Log of Spectroscopic Observations of SN 2018agk

| MJD | [a]Phase [days] | Telescope | Instrument | Exposure time [s] | Grism/Grating | Wavelength Range [Å] |
|---|---|---|---|---|---|---|
| 58,193.34 | −10.6 | HET | LRS2 | 2000 | Blue | 3640–6970 |
| 58,194.45 | −9.5 | Gemini-North | GMOS | $3 \times 900$ | R400 | 3957–8688 |
| 58,196.26 | −7.7 | du Pont | WFCCD | 1200 | Blue/red | 3500–9500 |
| 58,196.72 | −7.3 | HST | STIS | 2100 | G230L | 1570–3180 |
| 58,200.32 | −3.8 | HET | LRS2 | 1800 | Blue | 3640–6970 |
| 58,201.26 | −2.8 | NTT | EFOSC2 | $2 \times 900$ | gr11 + gr16 | 3340–10000 |
| 58,201.69 | −2.4 | HST | STIS | 2100 | G230L | 1570–3180 |
| 58,201.88 | −2.3 | HST | STIS | 800 | G430L | 2900–5700 |
| 58,201.90 | −2.2 | HST | STIS | 600 | G750L | 5240–10270 |
| 58,214.25 | +9.8 | NTT | EFOSC2 | 1500 | gr11 | 3340–7456 |
| 58,214.52 | +10.1 | FTS | FLOYDS | 3600 | … | 3146–10868 |
| 58,216.31 | +11.8 | NTT | EFOSC2 | 1500 | gr16 | 6000–10000 |
| 58,217.55 | +13.0 | FTS | FLOYDS | 3600 | … | 3146–10868 |
| 58,225.34 | +20.6 | FTN | FLOYDS | 3600 | … | 3146–10885 |
| 58,229.17 | +24.4 | NTT | EFOSC2 | $2 \times 1500$ | gr11 + gr16 | 3340–10000 |
| 58,233.32 | +28.4 | Shane | Kast | $4 \times 1200$ | 452/3306 + 300/7500 | 3306–10495 |
| 58,234.46 | +29.5 | FTN | FLOYDS | 3600 | … | 3146–10885 |
| 58,248.24 | +42.9 | FTN | FLOYDS | 3600 | … | 3146–10885 |
| 58,248.41 | +43.1 | Keck I | LRIS | $2 \times 1200$ | 600/4000 + 400/8500 | 3122–10147 |
| 58,287.09 | +80.8 | SOAR | Goodman | $2 \times 1800$ | 400 M1 + M2 | 3655–8896 |
| 58,310.30 | +103.4 | Keck I | LRIS | $2 \times 1200$ | 600/4000 + 400/8500 | 3122–10147 |

**Notes:** Uncertainties are in units of 0.001 mag.
[a] Phases relative to *B*-band maximum on MJD 58,204.178 according to SALT2 fit.

**Table 4**
Ground-based Optical Photometry of SN 2018agk

| MJD | [a]Phase (days) | *B* (mag) | *V* (mag) | *R* (mag) | *I* (mag) | *g* (mag) | *r* (mag) | *i* (mag) | Telescope/Observatory |
|---|---|---|---|---|---|---|---|---|---|
| 58,186.35 | −17.37 | … | … | … | … | … | … | 22.223(166) | DECam |
| 58,187.30 | −16.45 | … | … | … | … | 20.992(045) | … | … | DECam |
| 58,187.35 | −16.40 | … | … | … | … | … | … | 21.058(068) | DECam |
| 58,187.36 | −16.39 | … | … | … | … | … | … | 20.868(047) | DECam |
| 58,187.41 | −16.34 | … | … | … | … | … | … | 20.711(092) | DECam |
| 58,187.50 | −16.25 | … | … | … | … | 20.971(166) | 20.425(106) | … | PS1 |
| 58,187.56 | −16.19 | … | … | … | … | 20.683(232) | … | … | PS1 |
| 58,188.30 | −15.47 | … | … | … | … | 20.321(022) | … | … | DECam |
| 58,188.36 | −15.41 | … | … | … | … | … | … | 20.281(022) | DECam |
| 58,188.58 | −15.20 | … | … | … | … | 20.131(280) | … | … | PS1 |
| 58,193.12 | −10.78 | … | … | … | … | 18.062(006) | 18.014(007) | 18.068(010) | Swope |
| 58,193.15 | −10.75 | 18.237(039) | 18.006(048) | … | … | 18.182(034) | 18.021(042) | … | Las Cumbres |
| 58,193.17 | −10.73 | 18.174(014) | 18.014(017) | … | … | … | … | … | Swope |
| 58,193.37 | −10.53 | 18.045(041) | 17.989(052) | … | … | 18.088(034) | 17.768(044) | … | Las Cumbres |
| 58,193.40 | −10.50 | 18.165(015) | 17.997(016) | … | … | 17.988(012) | 17.935(014) | 17.987(019) | Swope |
| 58,194.23 | −9.69 | 17.996(025) | … | … | … | … | … | … | Las Cumbres |
| 58,194.24 | −9.68 | 17.970(026) | 17.907(029) | … | … | 17.884(024) | … | … | Las Cumbres |

**Table 4**
(Continued)

| MJD | [a]Phase (days) | B (mag) | V (mag) | R (mag) | I (mag) | g (mag) | r (mag) | i (mag) | Telescope/Observatory |
|---|---|---|---|---|---|---|---|---|---|
| 58,194.25 | −9.67 | ... | ... | ... | ... | 17.887(024) | 17.831(026) | 17.812(046) | Las Cumbres |
| 58,194.26 | −9.66 | ... | ... | ... | ... | ... | ... | 17.793(046) | Las Cumbres |
| 58,194.30 | −9.63 | 17.904(010) | 17.766(011) | ... | ... | 17.728(008) | 17.693(009) | 17.758(012) | Swope |
| 58,194.50 | −9.43 | ... | ... | ... | ... | 17.822(014) | ... | 17.772(013) | PS1 |
| 58,194.56 | −9.37 | ... | ... | ... | ... | 17.791(016) | ... | ... | PS1 |
| 58,195.26 | −8.69 | 17.752(010) | 17.585(010) | ... | ... | 17.609(007) | 17.513(008) | 17.650(010) | Swope |
| 58195.40 | −8.55 | ... | ... | ... | ... | 17.551(003) | ... | 17.668(002) | DECam |
| 58,195.45 | −8.50 | ... | ... | ... | ... | 17.668(012) | 17.578(010) | ... | PS1 |
| 58,195.52 | −8.44 | ... | ... | ... | ... | 17.565(012) | ... | ... | PS1 |
| 58,196.21 | −7.76 | 17.577(008) | 17.415(009) | ... | ... | 17.425(006) | 17.332(007) | 17.452(009) | Swope |
| 58,196.40 | −7.58 | ... | ... | ... | ... | 17.338(002) | ... | 17.503(002) | DECam |
| 58,196.45 | −7.53 | ... | ... | ... | ... | 17.511(026) | ... | ... | PS1 |
| 58,197.22 | −6.78 | 17.412(011) | 17.226(012) | ... | ... | 17.229(008) | 17.204(010) | 17.292(011) | Swope |
| 58,197.25 | −6.75 | 17.416(024) | 17.340(026) | ... | ... | 17.433(023) | 17.307(024) | 17.323(044) | Las Cumbres |
| 58,197.44 | −6.57 | ... | ... | ... | ... | 17.297(010) | 17.238(008) | ... | PS1 |
| 58197.54 | −6.47 | ... | ... | ... | ... | 17.317(010) | ... | ... | PS1 |
| 58199.02 | −5.03 | 17.209(050) | 17.081(034) | 16.704(083) | 16.702(067) | ... | ... | ... | Konkoly |
| 58,199.58 | −4.48 | ... | ... | ... | ... | 17.127(011) | ... | ... | PS1 |
| 58,200.08 | −3.99 | 17.097(031) | 17.271(040) | ... | ... | ... | ... | ... | Las Cumbres |
| 58,200.09 | −3.98 | ... | 17.046(037) | ... | ... | 17.126(031) | 17.174(035) | ... | Las Cumbres |
| 58,200.10 | −3.97 | ... | ... | ... | ... | ... | 17.065(032) | 17.019(055) | Las Cumbres |
| 58,200.20 | −3.88 | 17.133(010) | 17.010(012) | ... | ... | 17.005(007) | 16.915(009) | 17.147(011) | Swope |
| 58,201.25 | −2.85 | 17.066(011) | 16.917(011) | ... | ... | 16.907(010) | 16.744(022) | 17.094(011) | Swope |
| 58,202.05 | −2.07 | 17.083(035) | 16.942(032) | 16.625(043) | 16.770(058) | ... | ... | ... | Konkoly |
| 58,202.31 | −1.82 | ... | ... | ... | ... | 16.937(007) | 16.859(008) | 17.205(012) | Swope |
| 58,203.24 | −0.91 | 17.063(011) | ... | ... | ... | ... | ... | ... | Swope |
| 58,203.26 | −0.89 | 17.087(015) | 16.900(014) | ... | ... | 16.936(008) | 16.809(011) | 17.224(014) | Swope |
| 58,203.30 | −0.85 | 17.085(043) | 16.886(036) | ... | ... | 17.016(036) | 16.869(038) | 17.063(062) | Las Cumbres |
| 58,204.20 | +0.02 | ... | ... | 16.755(095) | 16.710(100) | ... | ... | ... | ANDICAM |
| 58,204.36 | +0.18 | 17.118(013) | 16.955(015) | ... | ... | 16.904(011) | 16.832(013) | 17.314(024) | Swope |
| 58,205.14 | +0.94 | 17.072(018) | 16.930(017) | ... | ... | 16.937(015) | 16.883(014) | 17.432(026) | Swope |
| 58,206.20 | +1.97 | 17.173(027) | 16.982(028) | ... | ... | 17.055(024) | 16.946(024) | 17.318(043) | Las Cumbres |
| 58,207.23 | +2.98 | ... | ... | 16.754(116) | 16.902(118) | ... | ... | ... | ANDICAM |
| 58,210.92 | +6.57 | 17.535(122) | 17.186(068) | 16.887(058) | 17.238(084) | ... | ... | ... | Konkoly |
| 58,211.21 | +6.85 | 17.397(030) | 17.101(030) | ... | ... | ... | ... | ... | Las Cumbres |
| 58,211.22 | +6.86 | ... | 17.075(029) | ... | ... | 17.221(025) | 17.049(027) | ... | Las Cumbres |
| 58,211.23 | +6.87 | ... | ... | ... | ... | ... | 17.091(027) | 17.524(049) | Las Cumbres |
| 58,211.23 | +6.88 | ... | ... | 16.995(113) | 17.085(080) | ... | ... | ... | ANDICAM |
| 58,211.87 | +7.50 | 17.480(096) | 17.135(037) | 16.803(064) | 17.305(131) | ... | ... | ... | Konkoly |
| 58,212.96 | +8.56 | 17.507(047) | 17.181(036) | 16.878(037) | 17.276(067) | ... | ... | ... | Konkoly |
| 58,215.07 | +10.62 | ... | ... | ... | ... | 17.346(004) | ... | ... | DECam |
| 58,215.13 | +10.67 | ... | ... | ... | ... | 17.385(003) | ... | ... | DECam |
| 58,215.18 | +10.72 | ... | ... | ... | ... | ... | ... | 18.091(005) | DECam |
| 58,215.31 | +10.85 | 17.745(031) | 17.288(030) | ... | ... | 17.486(025) | ... | ... | Las Cumbres |
| 58,215.32 | +10.86 | ... | ... | ... | ... | 17.485(028) | 17.367(029) | 17.942(058) | Las Cumbres |
| 58215.33 | +10.87 | ... | ... | ... | ... | ... | ... | 17.931(057) | Las Cumbres |
| 58,216.21 | +11.73 | 17.721(024) | 17.262(020) | ... | ... | 17.448(016) | 17.264(017) | 18.009(029) | Swope |
| 58,217.00 | +12.50 | 17.828(052) | 17.279(039) | 16.993(057) | 17.400(093) | ... | ... | ... | Konkoly |
| 58,217.17 | +12.66 | ... | ... | 17.420(095) | 17.431(092) | ... | ... | ... | ANDICAM |
| 58,217.25 | +12.74 | 17.888(019) | 17.377(015) | ... | ... | 17.571(014) | 17.359(015) | 18.018(026) | Swope |
| 58217.92 | +13.39 | 17.832(052) | 17.294(037) | 17.070(052) | 17.436(074) | ... | ... | ... | Konkoly |
| 58,218.90 | +14.35 | 18.166(048) | 17.530(036) | 17.384(052) | 17.617(084) | ... | ... | ... | Konkoly |
| 58,219.63 | +15.06 | 18.206(029) | 17.623(029) | ... | ... | ... | ... | ... | Las Cumbres |
| 58,219.64 | +15.07 | ... | 17.568(030) | ... | ... | 17.867(027) | 17.589(030) | ... | Las Cumbres |
| 58,219.65 | +15.08 | ... | ... | ... | ... | ... | 17.633(029) | 18.088(056) | Las Cumbres |
| 58,219.89 | +15.31 | 18.162(051) | 17.547(040) | 17.303(062) | 17.709(085) | ... | ... | ... | Konkoly |
| 58,220.42 | +15.83 | ... | ... | ... | ... | 17.801(015) | ... | 18.120(017) | PS1 |
| 58,220.48 | +15.89 | ... | ... | ... | ... | 17.837(015) | ... | ... | PS1 |
| 58,220.89 | +16.29 | 18.377(073) | 17.645(052) | 17.345(072) | 17.425(115) | ... | ... | ... | Konkoly |
| 58,221.28 | +16.67 | 18.355(021) | 17.619(014) | ... | ... | 17.925(015) | 17.524(013) | 18.042(020) | Swope |
| 58,221.41 | +16.79 | ... | ... | ... | ... | 17.920(015) | 17.594(011) | ... | PS1 |
| 58,221.89 | +17.26 | 18.535(060) | 17.684(047) | 17.333(057) | 17.691(081) | ... | ... | ... | Konkoly |
| 58,223.26 | +18.60 | 18.746(034) | 17.788(029) | ... | ... | 18.200(025) | 17.700(025) | 18.057(045) | Las Cumbres |
| 58,224.10 | +19.42 | 18.672(023) | 17.817(019) | ... | ... | 18.196(013) | 17.600(013) | 18.082(022) | Swope |

**Table 4**
(Continued)

| MJD | [a]Phase (days) | $B$ (mag) | $V$ (mag) | $R$ (mag) | $I$ (mag) | $g$ (mag) | $r$ (mag) | $i$ (mag) | Telescope/Observatory |
|---|---|---|---|---|---|---|---|---|---|
| 58,226.27 | +21.53 | 19.116(048) | 17.871(020) | ⋯ | ⋯ | 18.336(019) | 17.572(016) | 17.900(024) | Swope |
| 58,226.91 | +22.15 | 18.953(072) | 17.979(059) | 17.419(073) | 17.541(095) | ⋯ | ⋯ | ⋯ | Konkoly |
| 58,227.24 | +22.48 | 19.075(048) | 18.001(036) | ⋯ | ⋯ | 18.579(030) | ⋯ | ⋯ | Las Cumbres |
| 58,227.25 | +22.49 | ⋯ | ⋯ | ⋯ | ⋯ | 18.579(031) | 17.737(029) | 17.957(053) | Las Cumbres |
| 58,228.92 | +24.11 | 19.258(089) | 17.944(059) | 17.445(068) | 17.416(075) | ⋯ | ⋯ | ⋯ | Konkoly |
| 58,231.60 | +26.72 | ⋯ | 18.327(045) | ⋯ | ⋯ | ⋯ | ⋯ | ⋯ | Las Cumbres |
| 58,231.61 | +26.73 | ⋯ | 18.325(049) | ⋯ | ⋯ | 18.984(036) | 17.884(031) | ⋯ | Las Cumbres |
| 58,231.62 | +26.74 | ⋯ | ⋯ | ⋯ | ⋯ | ⋯ | 17.871(032) | 17.891(053) | Las Cumbres |
| 58,242.48 | +37.33 | ⋯ | ⋯ | ⋯ | ⋯ | ⋯ | 18.519(044) | ⋯ | Las Cumbres |
| 58,242.88 | +37.72 | ⋯ | 18.654(080) | 17.940(101) | 17.991(101) | ⋯ | ⋯ | ⋯ | Konkoly |
| 58,247.48 | +42.20 | 20.219(049) | 19.095(034) | ⋯ | ⋯ | 19.816(034) | 18.699(042) | 18.704(047) | Las Cumbres |
| 58,253.16 | +47.74 | 19.678(038) | 19.236(033) | ⋯ | ⋯ | ⋯ | ⋯ | ⋯ | Las Cumbres |
| 58,253.18 | +47.76 | ⋯ | 19.291(035) | ⋯ | ⋯ | 19.843(053) | 18.926(031) | 19.022(050) | Las Cumbres |
| 58,257.17 | +51.64 | ⋯ | ⋯ | ⋯ | ⋯ | ⋯ | 19.067(045) | ⋯ | Las Cumbres |
| 58,258.33 | +52.77 | ⋯ | ⋯ | ⋯ | ⋯ | 19.879(104) | 19.079(055) | ⋯ | PS1 |
| 58,258.40 | +52.84 | ⋯ | ⋯ | ⋯ | ⋯ | 19.779(080) | ⋯ | ⋯ | PS1 |
| 58,259.37 | +53.79 | ⋯ | ⋯ | ⋯ | ⋯ | 19.883(074) | ⋯ | 19.277(050) | PS1 |
| 58,260.34 | +54.73 | ⋯ | ⋯ | ⋯ | ⋯ | 19.728(059) | 19.150(031) | ⋯ | PS1 |
| 58,260.42 | +54.81 | ⋯ | ⋯ | ⋯ | ⋯ | 19.909(081) | ⋯ | ⋯ | PS1 |
| 58,261.00 | +55.38 | ⋯ | ⋯ | ⋯ | ⋯ | ⋯ | 19.259(048) | ⋯ | Las Cumbres |
| 58,272.15 | +66.24 | ⋯ | ⋯ | ⋯ | ⋯ | ⋯ | 19.488(045) | ⋯ | Las Cumbres |
| 58,272.16 | +66.25 | ⋯ | ⋯ | ⋯ | ⋯ | ⋯ | 19.619(050) | ⋯ | Las Cumbres |

**Notes.** Uncertainties are in units of 0.001 mag. This table has also been published in its entirety in a machine-readable format, including individual measurements and upper limits. A compact presentation is shown here for guidance regarding its form and content. Measurements with uncertainty greater than 0.3 mag are not included in this table.
[a] Phases relative to $B$-band maximum on MJD 58,204.178 according to SALT2 fit.

(This table is available in its entirety in machine-readable form.)

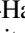**Table 5**
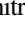Ground-based Infrared Photometry of SN 2018agk
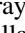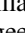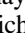
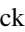| MJD | [a]Phase (days) | $H$ (mag) | $J$ (mag) | $K$ (mag) | Telescope |
|---|---|---|---|---|---|
| 58,204.20 | +0.02 | 17.220(252) | 16.937(107) | ⋯ | ANDICAM |
| 58,204.28 | +0.10 | 17.276(064) | 16.821(056) | 16.342(057) | SOFI |
| 58,207.23 | +2.98 | 17.694(189) | 17.313(237) | ⋯ | ANDICAM |
| 58,211.23 | +6.88 | 17.545(200) | 17.915(273) | ⋯ | ANDICAM |
| 58,216.11 | +11.62 | 17.590(064) | 17.813(081) | 16.765(070) | SOFI |
| 58,217.17 | +12.66 | 17.647(291) | 17.763(063) | ⋯ | ANDICAM |
| 58,231.17 | +26.31 | 17.439(066) | 17.687(081) | 16.830(085) | SOFI |
| 58,251.02 | +45.65 | 18.078(085) | 18.174(099) | 17.587(125) | SOFI |
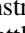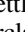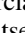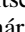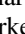
**Notes.** Uncertainties are in units of 0.001 mag.
[a] Phases relative to $B$-band maximum on MJD 58,204.178 according to SALT2 fit.

(This table is available in machine-readable form.)

### ORCID iDs

Qinan Wang ● https://orcid.org/0000-0001-5233-6989
Armin Rest ● https://orcid.org/0000-0002-4410-5387
Ryan Ridden-Harper ● https://orcid.org/0000-0003-1724-2885
Georgios Dimitriadis ● https://orcid.org/0000-0001-9494-179X
Gautham Narayan ● https://orcid.org/0000-0001-6022-0484
V. Ashley Villar ● https://orcid.org/0000-0002-5814-4061
Mark R. Magee ● https://orcid.org/0000-0002-0629-8931
Ryan J. Foley ● https://orcid.org/0000-0002-2445-5275
Edward J. Shaya ● https://orcid.org/0000-0002-3234-8699
Peter Garnavich ● https://orcid.org/0000-0003-4069-2817

Lifan Wang ● https://orcid.org/0000-0001-7092-9374
Lei Hu ● https://orcid.org/0000-0001-7201-1938
Attila Bódi ● https://orcid.org/0000-0002-8585-4544
Patrick Armstrong ● https://orcid.org/0000-0003-1997-3649
Katie Auchettl ● https://orcid.org/0000-0002-4449-9152
Thomas Barclay ● https://orcid.org/0000-0001-7139-2724
Geert Barentsen ● https://orcid.org/0000-0002-3306-3484
Zsófia Bognár ● https://orcid.org/0000-0002-8493-9781
Jamison Burke ● https://orcid.org/0000-0003-0035-6659
Kenneth Chambers ● https://orcid.org/0000-0001-6965-7789
David A. Coulter ● https://orcid.org/0000-0003-4263-2228
Maxime Deckers ● https://orcid.org/0000-0001-8857-9843

Jessie L. Dotson ◉ https://orcid.org/0000-0003-4206-5649
Lluís Galbany ◉ https://orcid.org/0000-0002-1296-6887
Santiago González-Gaitán ◉ https://orcid.org/0000-0002-4020-3457
Mariusz Gromadzki ◉ https://orcid.org/0000-0002-1650-1518
Michael Gully-Santiago ◉ https://orcid.org/0000-0002-4020-3457
Ottó Hanyecz ◉ https://orcid.org/0000-0002-9415-5219
Christina Hedges ◉ https://orcid.org/0000-0002-3385-8391
Daichi Hiramatsu ◉ https://orcid.org/0000-0002-1125-9187
Griffin Hosseinzadeh ◉ https://orcid.org/0000-0002-0832-2974
D. Andrew Howell ◉ https://orcid.org/0000-0003-4253-656X
Steve B. Howell ◉ https://orcid.org/0000-0002-2532-2853
Mark E. Huber ◉ https://orcid.org/0000-0003-1059-9603
Saurabh W. Jha ◉ https://orcid.org/0000-0001-8738-6011
David O. Jones ◉ https://orcid.org/0000-0002-6230-0151
Thomas B Lowe ◉ https://orcid.org/0000-0002-9438-3617
Steven Margheim ◉ https://orcid.org/0000-0001-8205-9441
Curtis McCully ◉ https://orcid.org/0000-0001-5807-7893
Ayan Mitra ◉ https://orcid.org/0000-0002-9436-8871
Jose A. Muñoz ◉ https://orcid.org/0000-0001-9833-2959
Matt Nicholl ◉ https://orcid.org/0000-0002-2555-3192
Jakob Nordin ◉ https://orcid.org/0000-0001-8342-6274
András Pál ◉ https://orcid.org/0000-0001-5449-2467
Yen-Chen Pan ◉ https://orcid.org/0000-0001-8415-6720
Anthony L. Piro ◉ https://orcid.org/0000-0001-6806-0673
Sofia Rest ◉ https://orcid.org/0000-0002-3825-0553
João Rino-Silvestre ◉ https://orcid.org/0000-0003-0793-3287
César Rojas-Bravo ◉ https://orcid.org/0000-0002-7559-315X
Krisztián Sárneczky ◉ https://orcid.org/0000-0003-0926-3950
Matthew R. Siebert ◉ https://orcid.org/0000-0003-2445-3891
Stephen J. Smartt ◉ https://orcid.org/0000-0002-8229-1731
Ken Smith ◉ https://orcid.org/0000-0001-9535-3199
Maximilian D. Stritzinger ◉ https://orcid.org/0000-0002-5571-1833
Róbert Szabó ◉ https://orcid.org/0000-0002-3258-1909
Róbert Szakáts ◉ https://orcid.org/0000-0002-1698-605X
Brad E. Tucker ◉ https://orcid.org/0000-0002-4283-5159
József Vinkó ◉ https://orcid.org/0000-0001-8764-7832
Xiaofeng Wang ◉ https://orcid.org/0000-0002-7334-2357
J. Craig Wheeler ◉ https://orcid.org/0000-0003-1349-6538
David R. Young ◉ https://orcid.org/0000-0002-1229-2499

## References

Arnett, W. D. 1982, ApJ, 253, 785
Astropy Collaboration, Price-Whelan, A. M., Sipőcz, B. M., et al. 2018, AJ, 156, 123
Baltay, C., Grossman, L., Howard, R., et al. 2021, PASP, 133, 044002
Barbary, K. 2016, Extinction V0.3.0, doi:10.5281/zenodo.804967
Barbary, K., Barclay, T., Biswas, R., et al. 2016, SNCosmo: Python library for supernova cosmology
Becker, A. 2015, HOTPANTS: High Order Transform of PSF ANd Template Subtraction
Bertin, E., Mellier, Y., Radovich, M., et al. 2002, in ASP Conf. Ser. 281, Astronomical Data Analysis Software and Systems XI, ed. D. A. Bohlender, D. Durand, & T. H. Handley (San Francisco, CA: ASP), 228
Blondin, S., Matheson, T., Kirshner, R. P., et al. 2012, AJ, 143, 126
Bose, S., Holoien, T., Dong, S., et al. 2018, TNSCR, 1, 501
Botyánszki, J., Kasen, D., & Plewa, T. 2018, ApJL, 852, L6
Branch, D., Dang, L. C., Hall, N., et al. 2006, PASP, 118, 560
Branch, D., Livio, M., Yungelson, L. R., Boffi, F. R., & Baron, E. 1995, PASP, 107, 1019
Brown, P. J., Dawson, K. S., Harris, D. W., et al. 2012, ApJ, 749, 18
Bulla, M., Miller, A. A., Yao, Y., et al. 2020, ApJ, 902, 48
Burns, C. R., Stritzinger, M., Phillips, M. M., et al. 2011, AJ, 141, 19
Buzzoni, B., Delabre, B., Dekker, H., et al. 1984, Msngr, 38, 9

Cartier, R., Sullivan, M., Firth, R. E., et al. 2017, MNRAS, 464, 4476
Chambers, K. C., Magnier, E. A., Metcalfe, N., et al. 2016, arXiv:1612.05560
Chonis, T. S., Hill, G. J., Lee, H., et al. 2016, Proc. SPIE, 9908, 99084C
Clemens, J. C., Crain, J. A., & Anderson, R. 2004, Proc. SPIE, 5492, 331
Conley, A., Sullivan, M., Hsiao, E. Y., et al. 2008, ApJ, 681, 482
Dan, M., Rosswog, S., Brüggen, M., & Podsiadlowski, P. 2014, MNRAS, 438, 14
Dan, M., Rosswog, S., Guillochon, J., & Ramirez-Ruiz, E. 2011, ApJ, 737, 89
DePoy, D., Abbott, T., Annis, J., et al. 2008, Proc. SPIE, 7014, 70140E
Dimitriadis, G., Foley, R. J., Rest, A., et al. 2019a, ApJL, 870, L1
Dimitriadis, G., Rojas-Bravo, C., Kilpatrick, C. D., et al. 2019b, ApJL, 870, L14
Dotson, J. L., Rest, A., Barentsen, G., et al. 2018, RNAAS, 2, 178
Eggleton, P. P. 1983, ApJ, 268, 368
Fink, M., Röpke, F. K., Hillebrandt, W., et al. 2010, A&A, 514, A53
Flaugher, B., Diehl, H. T., Honscheid, K., et al. 2015, AJ, 150, 150
Flewelling, H. A., Magnier, E. A., Chambers, K. C., et al. 2020, ApJS, 251, 7
Foley, R. J., Challis, P. J., Filippenko, A. V., et al. 2012, ApJ, 744, 38
Foley, R. J., Hoffmann, S. L., Macri, L. M., et al. 2020, MNRAS, 491, 5991
Foley, R. J., & Kirshner, R. P. 2013, ApJL, 769, L1
Foley, R. J., Narayan, G., Challis, P. J., et al. 2010, ApJ, 708, 1748
Foley, R. J., Pan, Y.-C., Brown, P., et al. 2016, MNRAS, 461, 1308
Foreman-Mackey, D. 2016, J. Open Source Software, 1, 24
Foreman-Mackey, D., Agol, E., Angus, R., & Ambikasaran, S. 2017, doi:10.5281/zenodo.1048287
Foreman-Mackey, D., Hogg, D. W., Lang, D., & Goodman, J. 2013, PASP, 125, 306
González-Gaitán, S., Conley, A., Bianco, F. B., et al. 2012, ApJ, 745, 44
Graham, M. L., Foley, R. J., Zheng, W., et al. 2015, MNRAS, 446, 2073
Guillochon, J., Dan, M., Ramirez-Ruiz, E., & Rosswog, S. 2010, ApJL, 709, L64
Haas, M. R., Batalha, N. M., Bryson, S. T., et al. 2010, ApJL, 713, L115
Hachisu, I., Kato, M., & Nomoto, K. 1996, ApJL, 470, L97
Harris, C. R., Millman, K. J., van der Walt, S. J., et al. 2020, Natur, 585, 357
Hayden, B. T., Garnavich, P. M., Kessler, R., et al. 2010, ApJ, 712, 350
Höflich, P., Wheeler, J. C., & Wang, L. 1999, ApJ, 521, 179
Hook, I. M., Jørgensen, I., Allington-Smith, J. R., et al. 2004, PASP, 116, 425
Hosseinzadeh, G., Sand, D. J., Valenti, S., et al. 2017, ApJL, 845, L11
Howell, S. B., Sobeck, C., Haas, M., et al. 2014, PASP, 126, 398
Hu, L., Chen, X., & Wang, J. 2021, ApJ, in press
Hunter, J. D. 2007, CSE, 9, 90
Iben, I., & Tutukov, J. A. V. 1984, ApJS, 54, 335
Jha, S. W., Maguire, K., & Sullivan, M. 2019, NatAs, 3, 706
Joyce, A., Jain, B., Khoury, J., & Trodden, M. 2015, PhR, 568, 1
Kasen, D. 2009, ApJ, 708, 1025
Kashi, A., & Soker, N. 2011, MNRAS, 417, 1466
Kashyap, R., Fisher, R., García-Berro, E., et al. 2015, ApJL, 800, L7
Kilpatrick, C. D., Foley, R. J., Drout, M. R., et al. 2018, MNRAS, 473, 4805
Kromer, M., Sim, S. A., Fink, M., et al. 2010, ApJ, 719, 1067
Kushnir, D., Katz, B., Dong, S., Livne, E., & Fernández, R. 2013, ApJL, 778, L37
Lentz, E. J., Baron, E., Branch, D., Hauschildt, P. H., & Nugent, P. E. 2000, ApJ, 530, 966
Levanon, N., & Soker, N. 2017, MNRAS, 470, 2510
Levanon, N., & Soker, N. 2019, ApJL, 872, L7
Levanon, N., Soker, N., & García-Berro, E. 2015, MNRAS, 447, 2803
Li, W., Wang, X., Vinkó, J., et al. 2019, ApJ, 870, 12
Li, X.-D., & Van den Heuvel, E. 1997, A&A, 322, L9
Livne, E., & Arnett, D. 1995, ApJ, 452, 62
Livne, E., & Glasner, A. S. 1991, ApJ, 370, 272
Maeda, K., Jiang, J.-a., Shigeyama, T., & Doi, M. 2018, ApJ, 861, 78
Maeda, K., Kutsuna, M., & Shigeyama, T. 2014, ApJ, 794, 37
Magee, M., Maguire, K., Kotak, R., & Sim, S. 2021, MNRAS, 502, 3533
Magee, M. R., & Maguire, K. 2020, A&A, 642, A189
Magee, M. R., Maguire, K., Kotak, R., et al. 2020, A&A, 634, A37
Magnier, E. A., Chambers, K. C., Flewelling, H. A., et al. 2020c, ApJS, 251, 3
Magnier, E. A., Schlafly, E. F., Finkbeiner, D. P., et al. 2020a, ApJS, 251, 6
Magnier, E. A., & Sweeney, W. E., Chambers, K. C., et al. 2020b, ApJS, 251, 5
Maoz, D., Mannucci, F., & Nelemans, G. 2014, ARA&A, 52, 107
Michaely, E., & Shara, M. M. 2021, MNRAS, 502, 4540
Miller, A. A., Cao, Y., Piro, A. L., et al. 2018, ApJ, 852, 100
Miller, A. A., Yao, Y., Bulla, M., et al. 2020, ApJ, 902, 47
Miller, J. S., & Stone, R. P. S. 1993, Lick Obs. Tech. Rep. 66, Lick Obs., Santa Cruz, CALick Obs
Moll, R., & Woosley, S. E. 2013, ApJ, 774, 137

Noebauer, U. M., Kromer, M., Taubenberger, S., et al. 2017, MNRAS, 472, 2787

Nojiri, S., Odintsov, S. D., & Oikonomou, V. K. 2017, PhR, 692, 1

Nomoto, K. 1982a, ApJ, 253, 798

Nomoto, K. 1982b, ApJ, 257, 780

Oke, J. B., Cohen, J. G., Carr, M., et al. 1995, PASP, 107, 375

Olling, R. P., Mushotzky, R., Shaya, E. J., et al. 2015, Natur, 521, 332

Pakmor, R., Kromer, M., Taubenberger, S., & Springel, V. 2013, ApJL, 770, L8

Pakmor, R., Zenati, Y., Perets, H. B., & Toonen, S. 2021, MNRAS, 503, 4734

Pan, Y. C., Foley, R. J., Jones, D. O., Filippenko, A. V., & Kuin, N. P. M. 2020, MNRAS, 491, 5897

Pereira, R., Thomas, R. C., Aldering, G., et al. 2013, A&A, 554, A27

Perets, H. B., Zenati, Y., Toonen, S., & Bobrick, A. 2019, arXiv:1910.07532

Perlmutter, S., Aldering, G., Goldhaber, G., et al. 1999, ApJ, 517, 565

Piro, A. L., & Morozova, V. S. 2016, ApJ, 826, 96

Piro, A. L., & Nakar, E. 2013, ApJ, 769, 67

Polin, A., Nugent, P., & Kasen, D. 2019, ApJ, 873, 84

Poznanski, D., Prochaska, J. X., & Bloom, J. S. 2012, MNRAS, 426, 1465

Prialnik, D., & Shara, M. M. 1986, ApJ, 311, 172

Priestley, M. B. 1981, Spectral analysis and time series: probability and mathematical statistics No. 04, QA280 (London: Academic Press), 7

Rest, A., Garnavich, P. M., Khatami, D., et al. 2018, NatAs, 2, 307

Rest, A., Scolnic, D., Foley, R. J., et al. 2014, ApJ, 795, 44

Rest, A., Stubbs, C., Becker, A. C., et al. 2005, ApJ, 634, 1103

Rest, A., Zenteno, A., Strampelli, G., et al. 2018, TNSTR, 346, 1

Riess, A. G., Casertano, S., Yuan, W., et al. 2018, ApJ, 861, 126

Riess, A. G., Casertano, S., Yuan, W., Macri, L. M., & Scolnic, D. 2019, ApJ, 876, 85

Riess, A. G., Filippenko, A. V., Challis, P., et al. 1998, AJ, 116, 1009

Riess, A. G., Macri, L. M., Hoffmann, S. L., et al. 2016, ApJ, 826, 56

Rodrigo, C., & Solano, E. 2020, Contributions to the XIV.0 Scientific Meeting (virtual) of the Spanish Astronomical Society, 182

Rodrigo, C., Solano, E., & Bayo, A. 2012, SVO Filter Profile Service Version 1.0, IVOA Working Draft 15 October 2012

Ruiter, A. J. 2020, IAU Symp., 357, 1

Schechter, P. L., Mateo, M., & Saha, A. 1993, PASP, 105, 1342

Schlafly, E. F., & Finkbeiner, D. P. 2011, ApJ, 737, 103

Scolnic, D., Casertano, S., Riess, A., et al. 2015, ApJ, 815, 117

Scolnic, D., Jones, D., Rest, A., et al. 2018, ApJ, 859, 101

Scolnic, D., Rest, A., Riess, A., et al. 2014, ApJ, 795, 45

Shappee, B., Holoien, T.-S., Drout, M., et al. 2018, ApJ, 870, 13

Shara, M. M., Livio, M., Moffat, A. F. J., & Orio, M. 1986, ApJ, 311, 163

Shaya, E. J., Olling, R., & Mushotzky, R. 2015, AJ, 150, 188

Smartt, S. J., Valenti, S., Fraser, M., et al. 2015, A&A, 579, A40

Smithsonian Astrophysical Observatory 2000, SAOImage DS9: A utility for displaying astronomical images in the X11 window environment

Soker, N. 2019, NewAR, 87, 101535

Stritzinger, M. D., Shappee, B. J., Piro, A. L., et al. 2018, ApJL, 864, L35

STScI Development Team 2013, pysynphot: Synthetic photometry software package

Tanikawa, A., Nakasato, N., Sato, Y., et al. 2015, ApJ, 807, 40

Tody, D. 1993, in ASP Conf. Ser. 52, Astronomical Data Analysis Software and Systems II, ed. R. J. Hanisch, R. J. V. Brissenden, & J. Barnes (San Francisco, CA: ASP), 173

Tucker, M. A., Shappee, B. J., & Wisniewski, J. P. 2019, ApJL, 872, L22

Valdes, F., & Gruendl, R. 2014, in ASP Conf. Ser., 485, Astronomical Data Analysis Software and Systems XXIII, ed. N. Manset & P. Forshay (San Francisco, CA: ASP), 379

Valenti, S., Sand, D., Pastorello, A., et al. 2014, MNRAS, 438, L101

Virtanen, P., Gommers, R., Oliphant, T. E., et al. 2020, Nature Methods, 17, 261

Wang, B., Li, X.-D., & Han, Z.-W. 2010, MNRAS, 401, 2729

Wang, X., Filippenko, A. V., Ganeshalingam, M., et al. 2009, ApJL, 699, L139

Waters, C. Z., Magnier, E. A., Price, P. A., et al. 2020, ApJS, 251, 4

Whelan, J., & Iben, I. J. 1973, ApJ, 186, 1007

Woosley, S. E., Taam, R. E., & Weaver, T. A. 1986, ApJ, 301, 601

Yang, Y., Hoeflich, P., Baade, D., et al. 2020, ApJ, 902, 46

Zenati, Y., Toonen, S., & Perets, H. B. 2019, MNRAS, 482, 1135